

## Review

# Properties of diamond-like carbon

J. Robertson

National Power Labs, Leatherhead, Surrey KT22 7SE (UK)

(Received August 9, 1991; accepted August 25, 1991)

### Abstract

This paper reviews the preparation and properties of hard forms of amorphous carbon and hydrogenated amorphous carbon, often known as diamond-like carbon. Properties such as the hydrogen content,  $sp^3$  content, optical gap, refractive index, hardness, elastic modulus and friction and their dependence on the deposition conditions are described. Models of the electronic structure and mechanical properties are used to relate the physical properties to the atomic structure.

### 1. Introduction

Carbon has two crystalline allotropes, diamond and graphite, which have very similar thermodynamic stability ( $\Delta G = 0.04$  eV at 300 K) but are separated by a large kinetic barrier. The strong directional  $sp^3$  bonding of diamond gives it many unique properties such as the highest elastic modulus, hardness and room temperature thermal conductivity of any solid [1–3], together with a large optical band gap and a very low thermal expansion coefficient, as summarized in Table 1. In contrast, the  $sp^2$  bonding of graphite gives it a layered structure and its weak interlayer bonding allows its use as a lubricant. The growth of polycrystalline diamond by vapour deposition and its unique properties have opened up a variety of applications as a high performance coating material, as recently reviewed by Angus and Hayman [1] and Bachmann [4]. However, further

improvements to the surface smoothness, growth rate and crystalline quality of the films are desirable before many of the applications can be fully realized.

Closely related vapour deposition methods can produce non-crystalline carbon films which are smooth, mechanically hard, IR transparent and chemically inert. These films are much easier to deposit than diamond and their properties are already sufficiently good for some immediate applications such as protective coatings for magnetic disk drives and antireflective protective coatings for IR windows [5]. Their desirable properties arise from the  $sp^3$  component of their bonding and have led to the name diamond-like carbon (DLC). This distinguishes them from more familiar forms of amorphous or glassy carbon formed by evaporation or pyrolysis, which are essentially all  $sp^2$  bonded as in graphite.

Diamond-like carbon was originally produced by ion beam deposition from a carbon arc source by Aisenberg

TABLE 1. Properties of various forms of carbon

	Density ( $gm\ cm^{-3}$ )	Hardness (GPa)	$Sp^3$ (%)	H (at.%)	Gap (eV)	Reference(s)
Diamond	3.515	100	100		5.5	[2]
Graphite	2.267		0		-0.04	
Glassy C	1.3–1.55	2–3	~0		0.01	
a-C (evaporated)	1.9–2.0	2–5	1		0.4–0.7	[29]
a-C (MSIB)	3.0	30–130	$90 \pm 5$	<9	0.5–1.5	[32, 39]
a-C:H (hard)	1.6–2.2	10–20	30–60	10–40	0.8–1.7	[12]
a-C:H (soft)	0.9–1.6	<5	50–80	40–65	1.6–4	[12, 59]
Polyethylene	0.92	0.01	100	67	6	[125]

and Chabot [6] and Spencer *et al.* [7]. It consists of a mixture of microcrystalline diamond and hydrogenated amorphous carbon (a-C:H). It is now known that diamond-like carbon can be produced by a wide range of methods [8, 9] such as ion beam deposition [6, 7, 10], plasma decomposition of hydrocarbons [9, 11–13], magnetron sputtering [14–16], ion beam sputtering [17, 18], ion plating [19, 20] and laser plasma deposition [21, 22], which tend to produce largely amorphous films. Nevertheless, these techniques produce forms of a-C(:H) with properties considerably poorer than those of diamond since they still contain considerable  $sp^2$  bonding and/or hydrogen [23–26]. Recently McKenzie and coworkers [27–32] have studied a form of a-C prepared by mass-selected ion beam (MSIB) deposition [33] which has 85%–90%  $sp^3$  bonding, minimal bonded hydrogen and properties much closer to those of diamond. This material is archetypal and shows that it is possible to prepare a tetrahedrally bonded form of a-C analogous to a-Si.

This paper reviews the deposition methods and properties of diamond-like carbon, particularly those properties relevant to coating applications. Models of the electronic structure and mechanical properties are introduced because these help to relate a wide range of properties to the underlying atomic structure and bonding.

## 2. Deposition methods

A wide variety of deposition methods have been used to prepare diamond-like carbon, as shown schematically in Fig. 1. A common feature of each method is the exposure of the growing film to bombardment by ions of medium energy, 20–500 V, which appears to promote  $sp^3$  bonding [6, 8]. The various systems and their growth rates are summarized in Table 2.

The first ion beam device of Aisenberg and Chabot [6] generated carbon ions by sputtering carbon electrodes in an argon atmosphere in a magnetically confined plasma. A bias voltage extracted the ions and directed them at the substrate. Higher growth rates were found to be possible if the ions were generated from a hydrocarbon source gas. Angus *et al.* [10] employed a thermionic cathode and an axial magnetic field to generate a plasma which could achieve high ionization rates in a source gas such as methane. Positive ions were extracted from the source by a bias electrode and directed at a substrate. The ions generated in the carbon source are of the form  $C_m^+$  while those from the gas source are of the form  $C_mH_n^+$ . In both cases the substrate also receives a large flux of neutral species such as un-ionized argon or methane from the background gas. This reduces the ion–neutral mass flux ratio to the order

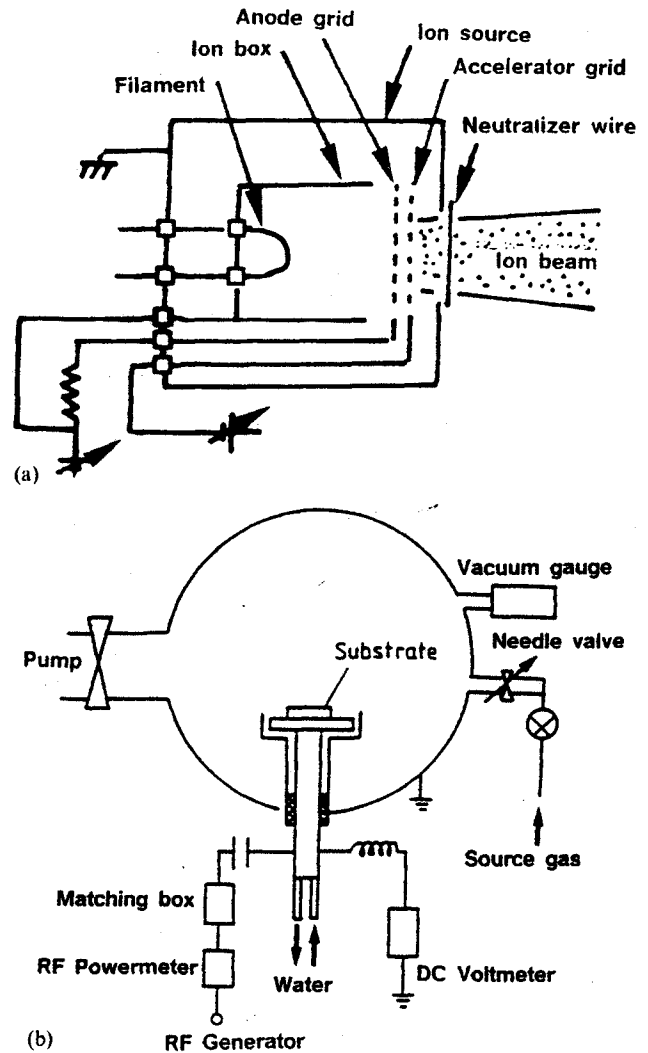


Fig. 1. Schematic diagrams of (a) ion beam deposition and (b) plasma deposition apparatus.

of 0.02 [9]. A high ionization ratio and a relatively high deposition rate can be achieved by using a cathodic arc as a carbon ion source [34].

A further increase in deposition rate is achieved by using a cascade arc source [35]. A highly ionized thermal plasma of methane and argon is created in an arc which is allowed to expand supersonically into a high vacuum towards the substrate. The degree of ionization is calculated to be high.

Deposition of a single ion species is possible if the ion beam is passed through a magnetic mass analyser for  $e/m$  selection. This filters neutrals, cluster species, graphitic fragments and impurities from the beam and allows only a pure beam of  $C^+$  (or  $C^-$ ) ions to reach the substrate. This MSIB method was first used by Aksenov *et al.* [33], who believed that a new phase of carbon was formed. It has now been used by a number of groups [27–33, 36–41]. Structural studies summarized

TABLE 2. Methods for the deposition of diamond-like carbon

	Precursor	Typical growth rate ( $\text{\AA s}^{-1}$ )	Reference(s)
Ion beam	Graphite	1.3	[6]
Ion beam	Methane	2	
PD	Methane	1	[12]
PD	Benzene	15	[12]
Ar beam sputtering	Graphite	3	[17]
Magnetron sputtering	Graphite	3	[14]
Ion plating	Benzene	10	[9]
Laser plasma	Graphite	<3	[22]
Cascade arc	Ar-methane	300	[35]
MSIB	Graphite	0.1-3	[36, 37]

later indicate that the resulting material is a form of a-C with the highest fraction of  $sp^3$  bonding of those from any present deposition process. The deposition rate for this method can be maximized by using the carbon arc as an ion source. The arc is confined magnetically for stability. The main practical problem with this method is the high compressive stress in the films, which limits adhesion.

Various sputtering methods can be used [14-18]. In ion beam sputtering, a beam of typically 1 kV  $\text{Ar}^+$  ions is directed at a graphite target. An angle of incidence of  $30^\circ$ - $45^\circ$  is used to maximize the yield. The sputtered carbon is condensed on a nearby substrate. A second  $\text{Ar}^+$  ion beam can be directed at the substrate to provide bombardment of the growing film. The advantage of ion beam sputtering is good process control while the disadvantage is low deposition rates due to the low sputter rate of graphite.

Higher deposition rates can be achieved by magnetron sputtering [14]. Here an argon plasma is used to both sputter from the target and bombard the growing film. Growth rates vary linearly with r.f. power and are typically  $3 \text{\AA s}^{-1}$ . Ion energies are of the order of 20 eV and these decline slowly with increasing power or gas pressure. A d.c. bias can be applied separately to the substrate if it is desired to raise the ion energy.

The most popular deposition method involves the r.f. plasma decomposition of a hydrocarbon source gas onto negatively self-biased substrates, as pioneered by Holland and Ojha [11]. Self-biasing is preferred to d.c. biasing because the films are usually insulating [9, 12, 13, 42-45]. In this method (Fig. 1(b)) the r.f. power is capacitively coupled to the substrate electrode and the counterelectrode is either a second electrode or just the grounded walls of the deposition chamber. This gives a large difference between the electrode sizes. If the r.f. frequency is greater than the ion plasma frequency, of the order of 2-5 MHz, the electrons can follow the r.f. voltage but the ions cannot. The large difference in electrode size and also in the electron and ion mobilities

produces a negative d.c. self-bias on the powered electrode, making it the cathode. The ion current is now largely d.c. while the compensating electron current flows in short bursts each r.f. cycle (Fig. 2). The d.c. bias is largely dropped across an ion sheath in front of the cathode and it accelerates the ions towards the cathode.

The bias voltage  $-V_b$  varies with r.f. power  $W$  and operating pressure  $P$  as

$$V_b = k \left( \frac{W}{P} \right)^{1/2} \quad (1)$$

where  $k$  depends on factors such as the electrode areas. The ion energy  $E_i$  depends on  $V_b$  and the ion mean free path in the sheath. At low pressures in the absence of collisions  $E_i \approx eV_b$ , while at typical gas pressures there is a spectrum of ion energies with a mean value of

$$E_i \approx k' V_b P^{-1/2} \quad (2)$$

or about  $E_i = 0.6V_b$  for a typical pressure of 3 Pa [12].

The deposition rate varies with the ionization potential and molecular weight of the source gas as shown in Fig. 3, with low ionization potentials and large molecular weights giving higher growth rates [12]. The deposition rate  $v$  for a given gas tends to vary with bias voltage and gas pressure as [12, 13, 42, 46, 47]

$$v = k'' V_b P \quad (3)$$

The total deposition flux again consists of both ions and neutral species from unionized background gas. Some of the neutral species can be energetic since they are formed by charge exchange with energetic ions. Catherine and Pastol [43] found the ion-neutral flux ratio to be between 0.1 and 0.2 for methane plasmas on the basis of ion flux measurements, while Lorcher and coworkers [48, 49] found a ratio closer to 0.5 for benzene plasmas by comparing with ion-beam deposited films.

Plasma deposition is also a popular method of preparing a-Si:H and polycrystalline diamond [4], but the conditions are considerably different in each case, as summarized in Table 3. Hard a-C:H is obtained if there

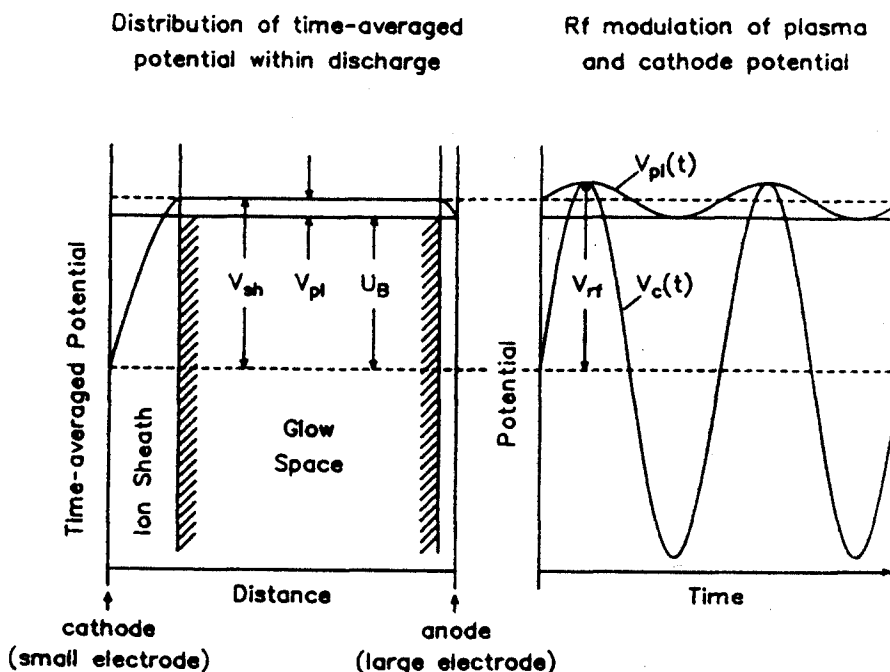


Fig. 2. Average potential distribution and r.f. waveforms in a capacitively coupled plasma reactor (after Koidl *et al.* [12]).

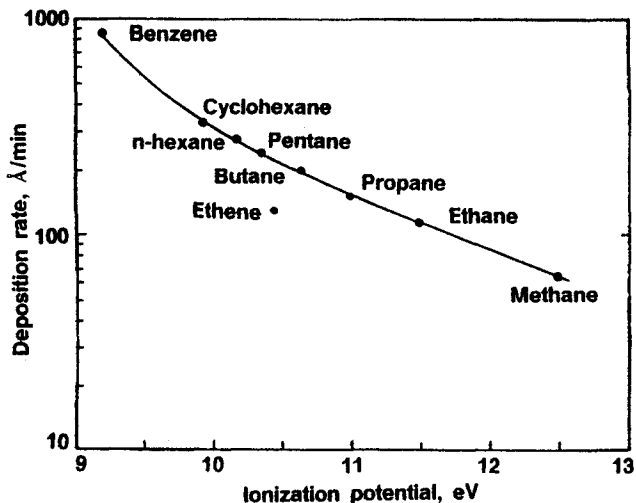


Fig. 3. Plasma deposition rate vs. source gas at 3 Pa and  $-400$  V bias (after Wagner *et al.* [48]).

TABLE 3. Conditions for plasma deposition of a-C:H, electronic grade a-Si:H and polycrystalline diamond

	a-C:H	a-Si:H	Diamond
R.f. power density ( $\text{W cm}^{-2}$ )	1	0.01	10
Gas pressure (Pa)	3	10	3
Substrate electrode	Cathode	Anode	
$T_d$ ( $^{\circ}\text{C}$ )	25	250	800
Dilution			$\text{H}_2:\text{CH}_4 = 100$

is ion bombardment during deposition, and these conditions are favoured by a cathodic substrate (to receive positive ions), a high r.f. power (for a high bias voltage), a low gas pressure (for high ionization) and low substrate temperatures (to minimize self-annealing). Electronic grade a-Si:H is deposited from silane plasmas under conditions which minimize the concentration of defect states due to silicon dangling bonds. Sufficient hydrogen must be retained to passivate the dangling bonds but not so much that polymeric  $\text{SiH}_2$  groups are common. This requires gentle conditions of a low r.f. power density, a moderate gas pressure and an anodic substrate (to minimize ion bombardment) and a substrate temperature of about  $250^{\circ}\text{C}$  to give optimum self-annealing. Diamond growth is favoured by using hydrogen-diluted source gases, a high power density and a higher substrate temperature. These conditions generate atomic hydrogen which suppresses the deposition of graphite and a-C by various mechanisms such as preferential etching [1]. It is interesting that the presence of atomic hydrogen and hydrogen dilution also promotes the deposition of microcrystalline silicon from silane discharges [50]. The atomic hydrogen is believed to ensure high surface mobilities for the depositing species by maintaining a hydrogen-terminated surface.

More highly ionized plasmas can be produced by using microwave discharges, particularly if operated at the electron cyclotron resonance [51]. This method produces high ion densities even at low gas pressures. The absence of electrodes and the ability to control the shape and position of the plasma make this method

technically attractive. Control of both ionization and ion energy can be achieved by using a microwave ion source and an r.f. self-biasing accelerator.

A carbon ion plasma can also be produced by the laser ablation of graphite [21, 22]. The resulting plasma probably resembles that formed by a cathodic arc. The resulting a-C is found to have a diamond-like character if the laser power density exceeds a threshold.

### 3. Structural overview

There are a great variety of non-crystalline carbons and hydrocarbons. They can be considered to have structures intermediate between those of diamond, graphite and hydrocarbon polymers in that they contain varying portions of  $sp^3$  carbon,  $sp^2$  carbon and hydrogen as summarized in Table 1. Angus and Hayman [1] and Angus [52] have proposed a valuable means of classifying these solids in terms of their atom density and hydrogen content as shown in Fig. 4. The atom number density is the total number of atoms per unit volume divided by Avogadro's number. This plot emphasizes that the diamond-like forms of a-C:H are unique in that they have a much higher atom density than conventional hydrocarbon polymers. Diamond is seen to have the highest atom density, and indeed has the highest atom density of any solid at ambient pressure. Graphite has a lower density and lower atom density than diamond. Amorphous carbon formed by evaporation or sputtering consists largely of  $sp^2$  carbon and has a density just less than graphite. The various conventional

hydrocarbon polymers included are the alkanes (AL) such as polyethylene, the polyacetylenes (AC) and the polynuclear aromatics (AR). The atom densities of diamond-like hydrocarbons are above  $0.19 \text{ (g atom) cm}^{-3}$ , indicating the effect of network cross-linking in raising the density. The hard amorphous carbons formed from filtered ion beams or from laser plasmas have densities and atomic densities between graphite and diamond.

### 4. Electronic structure

The beneficial properties of diamond arise from its  $sp^3$  bonding [1, 23]. At  $sp^3$  sites each of the four valence electrons of a carbon atom is assigned to a tetrahedrally directed  $sp^3$  hybrid which forms  $\sigma$  bonds to four adjacent carbon atoms. These bonds give diamond its rigidity and wide band gap. At  $sp^2$  sites, as in graphite, three of the valence electrons are assigned to trigonally directed  $sp^2$  hybrids which then form  $\sigma$  bonds such as the strong intralayer  $\sigma$  bonds of graphite. The fourth electron is placed in a  $p\pi$  orbital lying normal to the layer and this forms weaker  $\pi$  bonds which give rise to the anisotropic metallic character of graphite.

The electronic structure of an amorphous system can be described in terms of its density-of-electron-states spectrum, as shown schematically in Fig. 5 [23-26, 53, 54]. The Fermi level  $E_F$  separating the filled and empty states is placed at  $E=0$ . The  $\sigma$  bonds form the skeleton of the network. They give rise to a valence band of filled bonding ( $\sigma$ ) states lying at negative energies and a conduction band of empty antibonding ( $\sigma^*$ ) states, separated by a wide band gap of at least 5 eV. The  $\pi$  states form a filled  $\pi$  band and an empty  $\pi^*$  band which lie largely within the  $\sigma$ - $\sigma^*$  gap. The electronic structure of all amorphous carbons depends primarily on the  $\pi$  states because these states lie closest to  $E_F$ . They also tend to control the structure because states closest to  $E_F$  dominate changes in total energies, via perturbation theory.

It is possible to decouple the  $\pi$  and  $\sigma$  states and to treat their effects separately. The skeleton of  $\sigma$  bonds

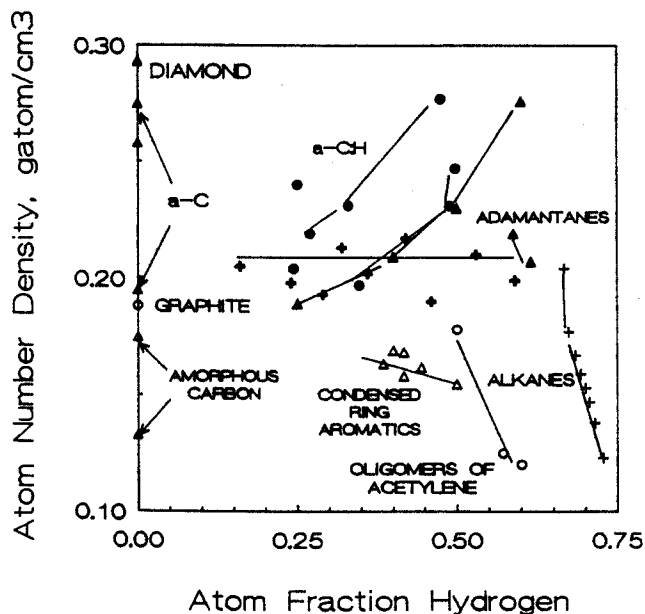


Fig. 4. Atom number density vs. atom fraction of hydrogen for solid carbons and hydrocarbons (after Angus and Hayman [1]).

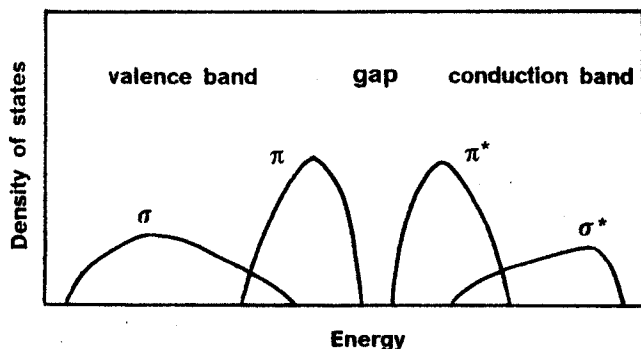


Fig. 5. Schematic electronic band structure of amorphous carbons.

consists of a series of two-centre bonds. Their total energy  $E_\sigma$  can be expressed as the sum of individual bond energies. The  $\pi$  electrons are more complicated since they can form both two-centre bonds, as in ethylene, and multicentre (resonant) bonds, as in benzene and graphite. Their bond energy  $E_\pi$  cannot in general be expressed as a sum of separate bond energies.


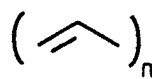
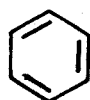
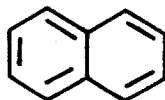
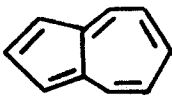

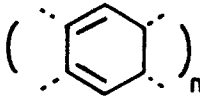
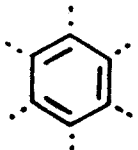
The  $\pi$  bond energy can be expressed in the Huckel model in terms of the normalized  $\pi$  bond energy  $E_\pi/\beta$ , where  $\beta$  is the nearest-neighbour  $\pi$  interaction,  $V(p\pi) \approx 2.9$  eV. The simplest configuration is the ethylenic double bond, C=C, which has  $E_\pi/\beta = 1$ . Such chain species are called olefinic.  $E_\pi$  is substantially increased by combining three C=C bonds into a planar sixfold or benzene ring (Table 4). Such ring species are called aromatic.  $E_\pi$  is further increased by fusing benzene rings into aromatic sheets and in this way aromatic clusters are built up.  $E_\pi$  is also larger for compact (graphitic) clusters than for linear (acenic) clusters. Ring orders except six are not generally favoured since they give states near  $E_F$ . However, adjacent pairs of five- and sevenfold rings, as in molecular azulene, are stable. Finally,  $\pi$ -bonded clusters tend to be planar because this keeps the  $\pi$  orbitals parallel and maximizes their interaction.

These results show that  $\pi$  bonding strongly favours aromatic rings over olefinic chains and also favours the clustering of separate rings into graphitic sheets. Thus aromatic ring clusters are expected to be the dominant species of  $sp^2$  sites. Also, for any given concentration of  $sp^2$  sites the  $sp^2$  sites have a strong tendency to segregate into sizable clusters rather than spread homogeneously throughout the sample. This is because  $E_\pi$  increases with cluster size while  $E_\sigma$  is insensitive to clustering. The stronger  $\sigma$  bonds therefore control the short-range order (SRO) of the network, the bond lengths and bond angles of the skeleton, while the  $\pi$  bonds introduce clustering or medium-range order (MRO) into the structure.

We are therefore led to a *two-phase model* of amorphous carbons [25] (Table 5). The first phase is the  $\pi$ -bonded clusters. These determine the electronic properties. This phase is embedded in a second phase. In evaporated or sputtered a-C the second phase is the minor phase and consists of a rim of defect or possibly  $sp^3$  sites which form a boundary between adjacent clusters. In a-C:H the second phase is the major  $sp^3$ -bonded matrix, which can be either a highly cross-linked network of  $sp^3$  sites, as in hard forms of a-C:H, or a more hydrogenated phase, as in softer, polymeric forms of a-C:H. The second phase largely determines the mechanical properties, as will be shown later.

A first-principles simulation of the electronic and atomic structure of a-C by Galli *et al.* [55] largely supports these results, finding a residual layer structure

TABLE 4.

	group	$E_{tot}/\beta$
	ethylene	1
	polyacetylene	1.273
	benzene	1.333
	naphthalene	1.368
	azulene	1.336
	quinoid	1.240
	polyacene	1.403
	graphite	1.616

for the  $sp^2$  sites but with considerable layer warping, cross-linking and intralayer disorder.

The optical gap of all amorphous carbons is determined by their  $\pi$  states since these states form both the valence and conduction band edges as seen in Fig. 5.

TABLE 5. Two-phase model of amorphous carbons

	Sp <sup>2</sup> phase	Sp <sup>3</sup> phase
a-C (evaporated)	Sheets	Sheet rims
a-C:H	Small clusters	Sp <sup>3</sup> or polymeric matrix
Control	Electronic properties	Mechanical properties

The optical gap  $E_g$  depends on the degree of clustering of the  $\pi$  states, *i.e.* the degree of MRO. The calculated band gap of compact clusters, the most stable sort, declines with  $M$ , the number of rings in the cluster, as [53]

$$E_g = \frac{2\beta}{M^{1/2}} \approx \frac{6}{M^{1/2}} \text{ eV} \quad (4)$$

where  $\beta$  is set to  $-2.9$  eV from fitting the  $\pi$  bands of graphite. This is equivalent to

$$E_g \approx \frac{7.7}{L_a} \text{ eV} \quad (5)$$

This contrasts with the situation in the more familiar  $\sigma$ -bonded amorphous semiconductors such as a-Si in which the band gap depends only on the SRO and is similar in the crystalline and amorphous phases.

The typical cluster sizes for various amorphous carbons can then be found from their gap and eqn. (1). Experimentally, the optical gap is usually defined by fitting the optical absorption coefficient  $\alpha$  to the Tauc formula

$$\alpha E = B(E - E_g)^2 \quad (6)$$

for  $\alpha > 10^4 \text{ cm}^{-1}$ . The absorption edges of sputtered a-C [56] and a hard a-C:H [57] shown in Fig. 6 are quite broad, indicating that a range of cluster sizes are present, each with its local band gap. The observed gap will therefore correspond not to that of an average cluster but to that of the largest significant clusters with the smallest gaps. For the sputtered a-C in Fig. 6  $E_g = 0.5$  eV corresponds to  $M = 140$  for the larger clusters and perhaps  $M = 35$  for a typical average cluster, corresponding to an in-plane correlation length of  $L_a \approx 9$  Å. For a hard a-C:H a typical gap of 1.2 eV corresponds to  $M = 25$  for the larger clusters and perhaps  $M = 6$  for a typical cluster, *i.e.*  $L_a = 3.8$  Å. For a soft a-C:H a gap of 2.5 eV gives  $M = 5$  and perhaps  $M = 2$  for a typical cluster.

## 5. Structure and electronic properties

A variety of techniques can be used to characterize the bonding in a-C or a-C:H, as reviewed critically elsewhere [25]. The most important parameters are the hydrogen content and the fraction of  $sp^3$ -bonded carbon sites. The hydrogen content can be found by nuclear

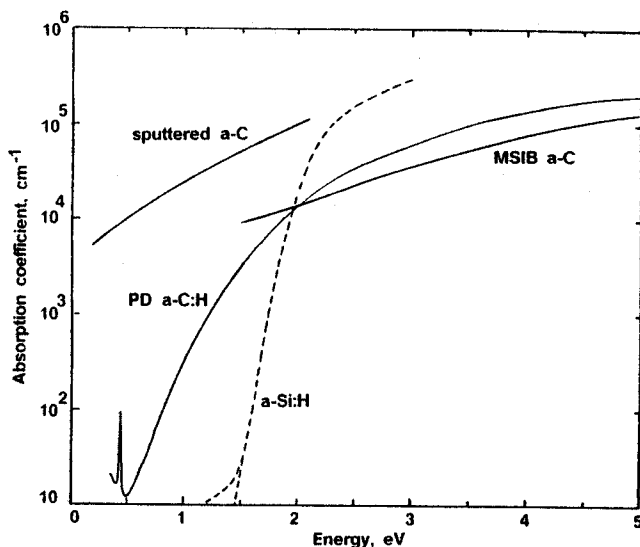


Fig. 6. Optical absorption edge of sputtered a-C (after Hauser [56]), a hard PD a-C:H (after Dischler *et al.* [57]) and MSIB a-C (after McKenzie *et al.* [31]).

reaction analysis (NRA) [12], elastic recoil detection (ERD) [46], nuclear magnetic resonance (NMR) [58] or analysis of the intensities of the C-H bond IR stretching modes [59, 60]. NRA, ERD and NMR can each give quantitative results, while IR requires the calibration of the oscillator strength. Thermal evolution must be used with care for a-C:H because hydrogen can evolve from a-C:H as hydrocarbons as well as  $H_2$ .

Estimation of the  $sp^3$  fraction is more problematic. The two most reliable direct methods are NMR and electron energy loss spectroscopy (EELS).  $Sp^2$  and  $sp^3$  sites give distinct chemically shifted peaks in the NMR spectrum whose intensity is proportional to their concentration [58, 61–65]. In combination with proton decoupling, it is also possible to determine the fraction of hydrogenated and unhydrogenated sites in each case [58]. High energy EELS, also known as X-ray near-edge spectroscopy (XANES), is the absorption spectrum of a carbon 1s core electron excited into empty conduction band states. The spectrum consists of a peak at 285 eV due to transitions from the 1s core level to empty  $2p\pi^*$  states on  $sp^2$  sites and a broad peak around 290 eV due to transitions to empty  $\sigma^*$  states of  $sp^3$ ,  $sp^2$  and hydrogen sites [15, 28, 65–68]. The relative intensities of the 285 and 290 eV peaks are proportional to the relative concentrations of  $\pi$  and  $\sigma$  electrons if suitably calibrated to those of graphite and diamond. Care must be taken in collecting the  $\pi^*$  electrons from graphite since the emission is strongly anisotropic and accounts for the different spectra shown by various authors.

Mass density also gives very useful indirect information on the likely  $sp^3$  content of a-C owing to the large difference in the densities of graphite (2.267) and diamond

(3.515). The  $sp^3$  content can then be inferred by interpolation. Density is less meaningful in a-C:H since its polymeric bonding component can give densities down to 0.92, that of polythene, but nevertheless, high densities correspond to favourable properties. Density can be measured by flotation [29], weight gain measurements during deposition [12, 15] or Rutherford backscattering (RBS) [46] or be inferred from EELS. The EELS method uses low energy EELS which shows a peak at 22–35 eV due to the plasma oscillations of all the valence electrons, known as the  $\sigma + \pi$  valence plasmon. Its energy  $E_p$  is given by

$$E_p = \hbar \left( \frac{Ne^2}{m\epsilon_0} \right)^{1/2} \quad (7)$$

where  $N$  is the number of valence electrons per cubic metre. An effective electron mass  $m$  slightly different from the free-electron mass must be used for  $E_p$  of graphite or diamond to agree with its free-electron value. Wang *et al.* [67] found a reasonable correlation between densities deduced from  $E_p$  and those measured by flotation.

$Sp^3$  contents can also be deduced from IR spectra [59, 60] or optical spectra [14, 66, 68], but these techniques are now felt to be less reliable [69–71]. In the IR method the bonding ratio is derived from the relative strengths of the  $sp^3$  and  $sp^2$  C–H vibration bands at  $2000 \text{ cm}^{-1}$ . However, this method assumes that all sites are hydrogenated, but NMR shows that this is not so [64]. Auger spectra have also been used [72] but need further consideration.

Raman spectroscopy is often used to characterize the crystallinity of diamond thin films [73] and graphitic carbons [74]. The Raman spectrum of crystalline diamond consists of a single sharp peak at  $1332 \text{ cm}^{-1}$ . The Raman spectrum of graphitic carbon consists of two peaks: the G peak centred on  $1550 \text{ cm}^{-1}$  is the zone centre  $E_{2g}$  mode of the perfect graphite crystal and the D peak centred on  $1350 \text{ cm}^{-1}$  is a zone edge  $A_{1g}$  mode which is activated by disorder [74]. The D mode is a common feature of all disordered graphitic carbons (coals, glassy carbon, etc.) whose intensity relative to the G peak has been shown to vary inversely with the size of the graphite crystallites as [74, 75]

$$\frac{I(D)}{I(G)} = \frac{k}{L_a} \quad (8)$$

The overall Raman spectrum of mixed  $sp^2$ – $sp^3$ -bonded carbons tends to be dominated by the  $sp^2$  component because the Raman cross-section of the G mode is 30–60 times that of the  $1332 \text{ cm}^{-1}$  diamond mode [76].

Figure 7 shows typical Raman spectra of plasma-deposited (PD) a-C:H and sputtered and evaporated a-C [77, 78]. Each spectrum can be decomposed into Gaussians centred around the positions of the G and D

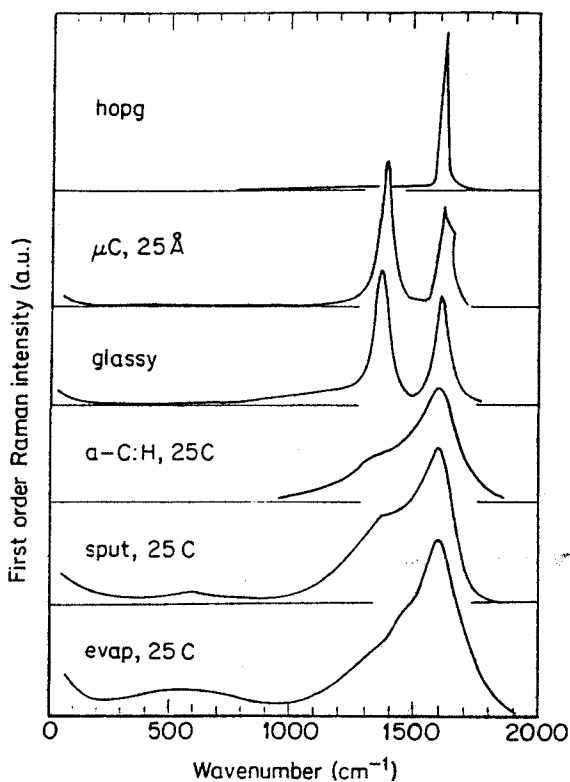


Fig. 7. Raman spectrum of graphite and typical spectra of microcrystalline graphite, PD a-C:H [78], sputtered a-C and evaporated a-C [77].

modes. Values of  $I(D)/I(G)$  greater than unity are often found in a-C and a-C:H [77–80]. The presence of a large D component suggests that the  $sp^2$  cluster model is basically correct.

The  $I(D)/I(G)$  ratio is often used to derive an  $sp^2$  correlation length for a-C(:H). Tamor *et al.* [79] noted that both  $I(D)/I(G)$  and the optical gap depend on  $L_a$ , according to theory. They found that  $I(D)/I(G)$  increased with increasing bias voltage for PD a-C:H, implying that  $L_a$  falls with increasing bias from eqn. (8). They also noted that the gap decreased with increasing  $V_b$ , implying that  $L_a$  increases with increasing bias from eqn. (5). They suggested that eqn. (8) fails in the limit of small  $L_a$ . Instead,  $I(D)/I(G)$  follows a dependence as shown in Fig. 8, reaching a peak around  $12 \text{ \AA}$  and then declining at lower  $L_a$ . This seems reasonable:  $I(D)$  cannot increase without limit at small  $L_a$ . The Raman spectrum of an amorphous solid equals the phonon density of states (DOS) weighted by the Raman-scattering matrix element. Clearly  $I(D)$  can increase to the maximum set by the phonon DOS around the K point of the Brillouin zone.  $I(D)$  may then be forced to decrease again for  $L_a < 12 \text{ \AA}$  since the density of states is forced into modes away from K with smaller matrix elements.

The Raman spectrum has also been used to deduce an  $sp^3$  fraction [15, 21]. Richter *et al.* [21], noting that



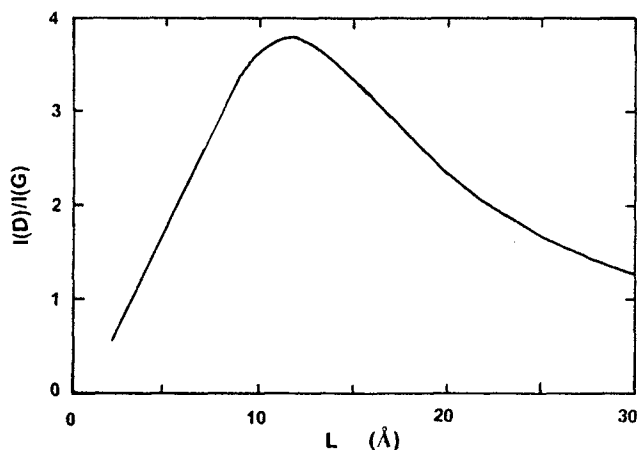


Fig. 8. Expected variation of normalized Raman D mode intensity  $I(D)/I(G)$  with in-plane correlation length  $L_a$ .

the G peak is red shifted towards its position in diamond in random network simulations [81], took the  $sp^3$  fraction to be proportional to this shift. This method seems unreliable, firstly because the G shift depends on the excitation frequency and secondly because the shift is zero for PD a-C:H deposited at  $V_b = 1$  kV, which is known from NMR to still contain a 20%  $sp^3$  fraction.

The local structure can also be measured by electron, X-ray or neutron diffraction [82–87]. The results of such efforts are discussed individually.

### 5.1. a-C

Graphite consists of hexagonal layers of  $sp^2$  sites stacked in an ABAB... sequence with an interlayer spacing of 3.35 Å. Glassy carbon formed by the pyrolysis of various organic materials consists of convoluted graphitic sheets of  $sp^2$  sites. The structure factor (diffraction pattern) of glassy carbon shown in Fig. 9 indicates a strong retention of the graphitic structure within each layer [82] (Table 6). The in-plane correlation length  $L_a = 15$  Å and the interplane correlation length  $L_c = 5–15$  Å are quite large, suggesting that glassy carbon should not be regarded as a true amorphous or glassy solid. It has a lower macroscopic density than graphite owing to microvoids.

a-C prepared by the electron beam evaporation of graphite or from graphite electrodes also consists of nearly 100%  $sp^2$  sites (Table 1). This is most clearly seen in its EELS spectrum (Fig. 10) in which its 285 eV peak is of similar size to the angle-averaged peak of graphite [28, 66]. Diffraction studies tend to reach similar conclusions [29, 83, 84]. The density of roughly 2.0 is also consistent with  $sp^2$  bonding.

The structure of sputtered a-C has been studied by neutron diffraction by Li and Lannin [87]. This material was prepared by condensing on liquid-nitrogen-cooled substrates to minimize any heating-induced graphitiza-

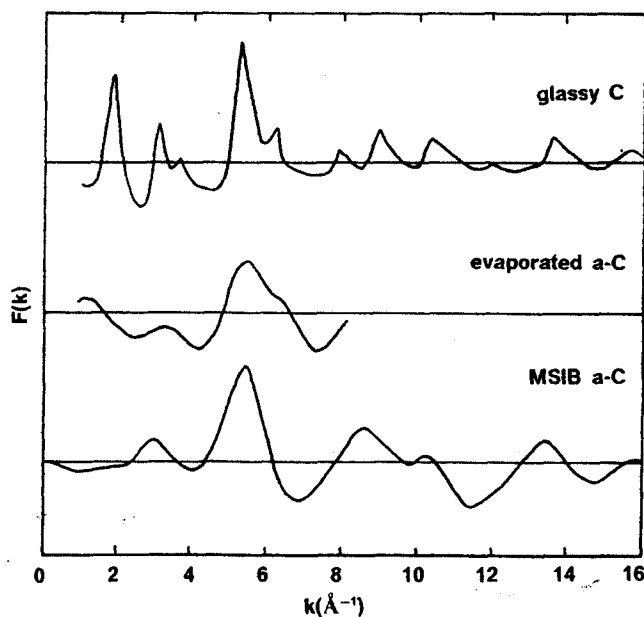


Fig. 9. Structure factors of glassy carbon [82], evaporated a-C [83] and MSIB a-C [32].

tion. Its density is similar, 2.0, but a higher local density was deduced from its radial distribution function (RDF). The RDF is the probability of finding an atom at a given distance from another atom and is shown in Fig. 11. The first peak due to nearest neighbours lies at  $r_1 = 1.46$  Å and contains  $n_1 = 3.3$  atoms (Table 7). These values and the density are consistent with 10%–20%  $sp^3$  bonding. The second peak at  $r_2 = 2.49$  Å gives a bond angle of  $117^\circ$  and contains 6.9 atoms, compared to  $120^\circ$  and  $n_2 = 6$  respectively for  $sp^2$  bonding. A sixfold ring in graphite has a cross-ring distance of 2.84 Å. The absence of a peak at this distance was used as evidence against a disordered graphitic structure for this form of a-C. However, this peak only contains two atoms and is easily washed out by the presence of 5%–10% five- and sevenfold rings, as is the analogous third-neighbour peak in a-Ge. Recent NMR data [88] on this sputtered a-C found 94%  $sp^2$  and 6%  $sp^3$  bonding, similar to that deduced by EELS for evaporated a-C. EELS also suggests a high proportion of  $sp^2$  sites in magnetron-sputtered a-C [15]. In the opinion of the author, these results and the discussion of the nature of the 2.84 Å RDF peak suggest that sputtered and evaporated a-C are predominantly  $sp^2$  bonded and locally layered, but with more layer warping, cross-linking and intralayer disorder than in glassy carbon.

Figure 6 shows the optical absorption spectrum of sputtered a-C from Hauser [56]. The optical gap is 0.5 eV. Optical gaps in the range 0.4–0.7 eV were found by Savvides [14] and Cho *et al.* [15], with the optical gap and  $sp^3$  content increasing as the r.f. power decreases. Gaps and densities were found to vary inversely with

TABLE 6. Peak positions in  $F(k)$  of various forms of a-C compared to the indexed reflections of graphite and diamond

	Peak position ( $\text{\AA}^{-1}$ )							
Glassy C	1.8	2.98		5.11	5.96	7.8	8.8	10.2
a-C (evaporated)	1.0	2.9		5.1		8.7	10.3	
a-C (sputtered)	1.6	2.95		5.5		8.7	10.5	
a-C (MSIB)	1.2	2.9		5.4		8.7	10.3	
Graphite ( <i>hkl</i> )	(002)	(100)		(110)	(200)	(210)	(300)	(220)
	1.88	2.95		5.11	5.90	7.82	8.86	10.2
Diamond ( <i>hkl</i> )		(100)	(200)	(220)	(311)	(331)		
		3.06	3.53	5.00	5.86	7.71		

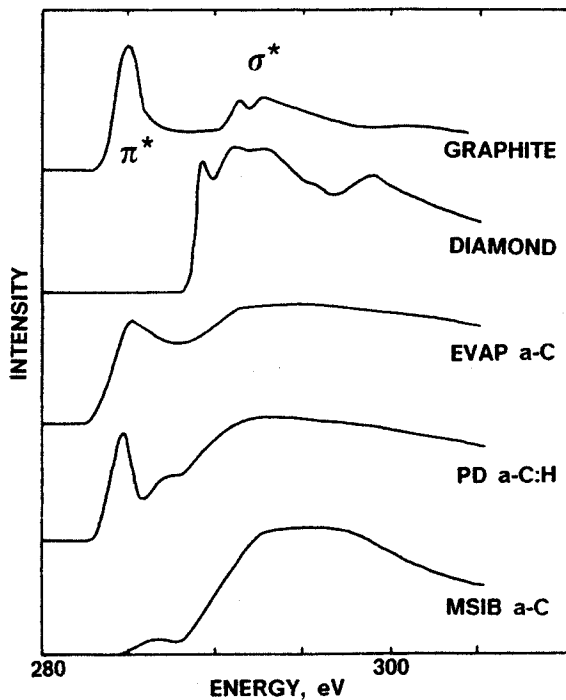
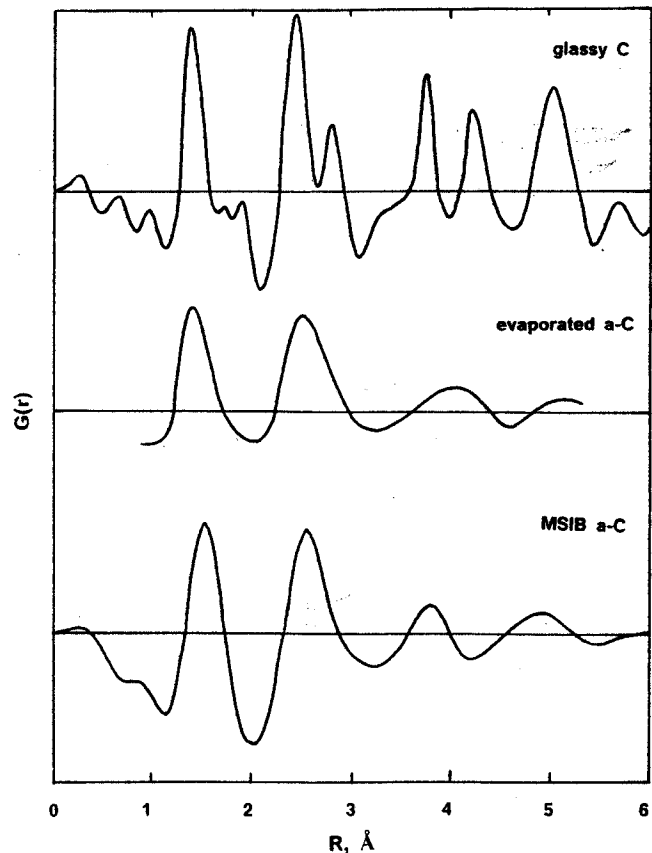
Fig. 10. EELS spectra of graphite, diamond, evaporated a-C, a-C:H and MSIB a-C (after Berger *et al.* [28] and Fink *et al.* [66]).

Fig. 11. Radial distribution functions of glassy carbon, evaporated a-C and MSIB a-C.

gas pressure by Rossnagel *et al.* [16], reaching quite high values of 2.1 eV and 2.8 at the lowest pressures where the degree of ionization is highest.

As yet there has been no thorough study of the variation in the properties of sputtered or ion beam a-C with ion energy  $E_i$ . In general, Angus *et al.* [8] note that the hardness and diamond-like character of a-C depend strongly on  $E_i$  passing through a maximum at moderate ion energies. At low  $E_i$  a-C is "graphitic" and not particularly hard, like evaporated a-C, while at high  $E_i$  it becomes less hard again and has a highly disordered graphitic structure.

Cuomo *et al.* [18] sputtered a-C on a series of increasingly well heat-sunk substrates. They estimated both the  $sp^3$  content and density from EELS. They found that the  $sp^3$  content increased strongly with increasing thermal conductivity of the substrate material. This result is

significant in terms of the deposition mechanism because of the low ion energies present during deposition, although the deposition rate involved,  $8 \text{ \AA min}^{-1}$ , is low.

The structure of highly tetrahedral a-C prepared by MSIB has been deduced by a variety of methods. A density of 2.85 was measured by flotation [30], while the bulk valence plasmon energy of 32 eV gives a local density of order 3.1, approaching that of diamond [30]. Its EELS spectrum (Fig. 10) shows only a small peak at 285 eV, consistent with about 15%  $sp^2$  bonding [28]. Its structure has been measured by neutron diffraction

TABLE 7. Interatomic distances ( $r$ ), coordination numbers ( $n$ ) and densities of various forms of carbon

	$r_1$ (Å)	$n_1$	$r_2$ (Å)	$n_2$	Local density (gm cm <sup>-3</sup> )	Reference
Graphite	1.42	3	2.45	6	2.267	
Diamond	1.544	4	2.512	12	3.515	[2]
Glassy C	1.425	2.99	2.45	6.1	1.49	[82]
a-C (evaporated)	1.43	3.3	2.53	8.8	2.0	[29]
a-C (sputtered)	1.46	3.34	2.49	6.7	2.44	[87]
a-C (MSIB)	1.526	3.9	2.52	8.9–10.9	3.0	[32]
a-C:H	1.49	2.5				[86]

[32] and earlier by electron diffraction [30]. Figure 11 compares the RDF of MSIB a-C from neutron diffraction with that of glassy carbon [82] and evaporated a-C [83]. The first peak distance of 1.53 Å is consistent with 10%  $\pm$  5% sp<sup>2</sup> bonding. The peak sizes are less reliable indicators of coordinations in this particular material owing to the scattering effect of a small (about 9%) amount of non-bonded hydrogen. This hydrogen appears to be present as H<sub>2</sub> at voids or microvoids rather than as C–H bonds, since the latter interpretation would give a poorer fit to the RDF. It is interesting that the structure factors of MSIB a-C and glassy carbon in Fig. 9 are superficially similar in peak positions, etc. (Table 6), indicating the degree of analysis needed to differentiate structures.

Figure 6 shows the optical absorption spectrum of MSIB a-C from McKenzie *et al.* [31]. The spectrum has a strong tail down to 1.5 eV which can only be due to  $\pi$  states at sp<sup>2</sup> sites. The spectrum does not fit the Tauc form, so that gaps from 1.3 to 3.5 eV can be found by fitting different parts of the optical absorption curve. The  $E_{04}$  gap is 3.5 eV, consistent with predominantly sp<sup>3</sup> bonding. The electrical gap appears to be similar. However, the absorption only falls very gradually within the gap. This absorption must be attributed to  $\pi$  states. Lower optical gaps of 0.5–1.5 eV were quoted by Ishikawa *et al.* [40].

The dependence of the properties of MSIB a-C on ion energy can be studied by applying a bias voltage to the ion gun. McKenzie *et al.* [31] found that its density passed through a peak at ion energies of the order of 30 eV, as shown in Fig. 12. They also found that the films were under large compressive strains, which were deduced from substrate curvature. They found the density and strain variations to be strongly correlated [31]. Koskinen [37] and Ishikawa *et al.* [40] also found that the density and other properties passed through a peak with ion energy, although at a much higher energy of 150–300 eV (Fig. 12). The reason for this difference from McKenzie *et al.*'s results is not known. Ishikawa *et al.* used C<sup>-</sup> ions.

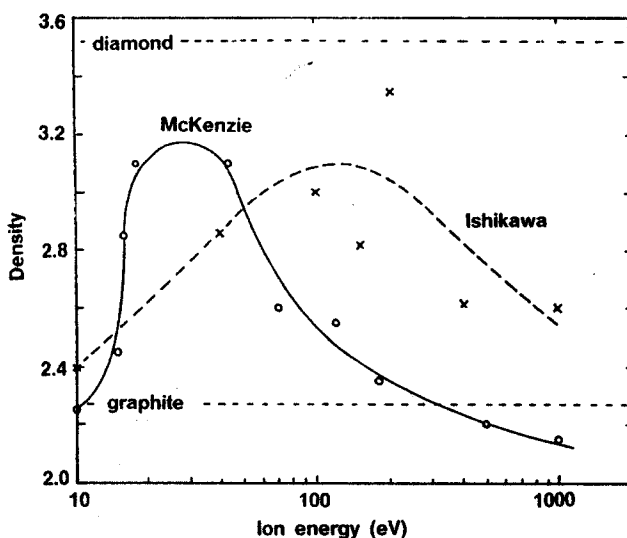


Fig. 12. Density vs. ion energy for MSIB a-C (from McKenzie *et al.* [31], Koskinen [37] and Ishikawa *et al.* [40]).

### 5.2. a-C:H

The properties of a-C:H depend primarily on the mean ion energy  $E_i$ . In the case of PD a-C:H they depend on the negative substrate bias voltage  $V_b$ . Figure 13 shows the variation of hydrogen content and sp<sup>3</sup> fraction with bias voltage for films deposited from methane and benzene at room temperature. The hydrogen content was derived from NMR data for the methane films of Tamor *et al.* [64] and was measured by NRA for the benzene films of Koidl *et al.* [12]. The hydrogen content is seen to decline rapidly with increasing bias, there being a similar variation for each type of film despite the different measurement techniques. Interestingly, a much lower hydrogen content is found in films deposited from acetylene [47]. The sp<sup>3</sup> fraction was measured by NMR. This also declines with increasing bias.

These variations lead to three regimes of properties [12]. At low bias the bonding is dominated by =CH<sub>2</sub> groups and the properties are rather polymeric, giving "soft" a-C:H. At intermediate bias the decline in

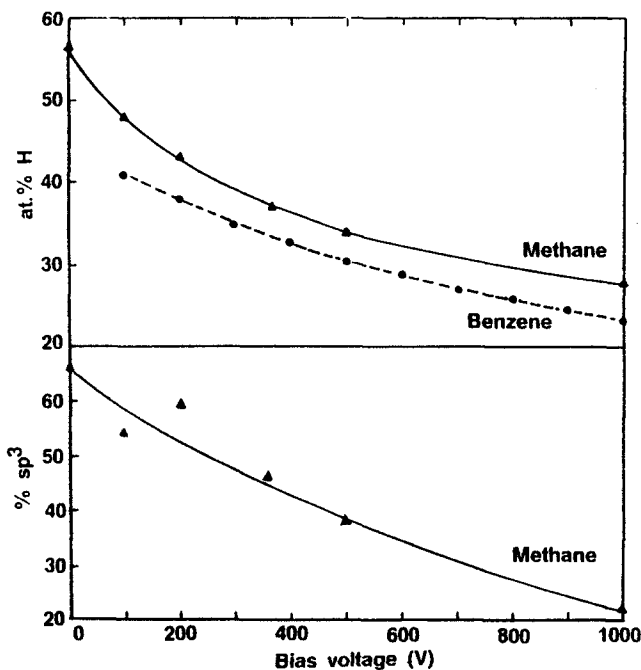


Fig. 13. Hydrogen content and  $sp^3$  fraction vs. bias voltage for PD a-C:H from benzene (after Koidl *et al.* [12]) and methane source gases (after Tamor *et al.* [64]).

hydrogen content gives the films their most “diamond-like” character. This regime of “hard” a-C:H extends from about 100 V to 1 kV for methane films and from 200 V to 1.2 kV for benzene films. Finally,  $sp^2$  bonding predominates at the highest bias, where the structure is highly disordered graphitic.

The optical gap is found to vary in a very similar fashion for a-C:H derived from both methane [79, 89] and benzene [12] (Fig. 14). The gap declines rapidly with bias, from 2.5–3.5 eV at  $V_b=0$  to 1.0 eV at  $V_b=$

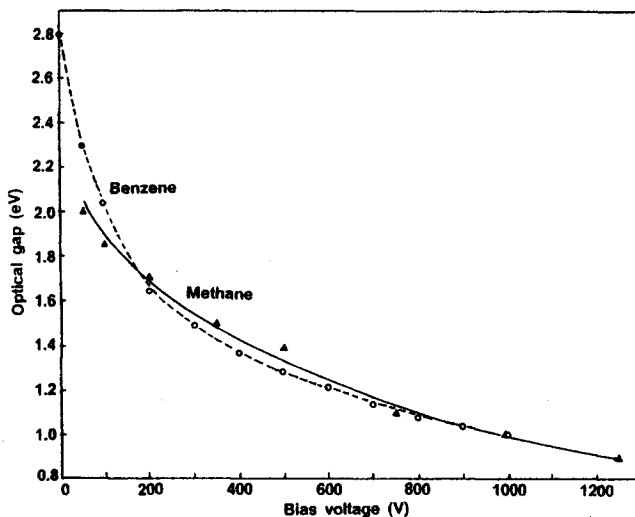


Fig. 14. Optical gap vs. bias voltage for PD a-C:H from methane and benzene source gases (after Tamor [79, 89] and Koidl *et al.* [12]).

1 kV. Hard a-C:H has  $E_g < 1.6$  eV. Figure 15 shows the variation in refractive index with bias for PD a-C:H deposited from benzene [12]. It increases with bias.

The mass density of methane-deposited a-C:H has been measured by Catherine and Couderc [42], Zou *et al.* [46] and Wang *et al.* [67] with broadly similar results. Figure 16 shows the variation in mass density with bias for both the methane films of Tamor [89] and the benzene films of Koidl *et al.* [12]. Both were determined by weight gain. The density is seen to increase continuously with increasing bias for the benzene films but to pass through a peak for the methane films.

Figure 17 shows the variation in hardness  $H$ , as measured by a nano-indenter, with bias for both the methane films of Jiang *et al.* [90] and the benzene films of Koidl *et al.* [12].  $H$  is very low at  $V_b=0$  V for soft a-C:H. It then increases and passes through a maximum at around 200 V for the methane films whereas it increases continuously for the benzene films. The data of Weissmantel *et al.* [91] suggest that  $H$  declines again above 1–1.5 kV, as shown dashed in Fig. 17.

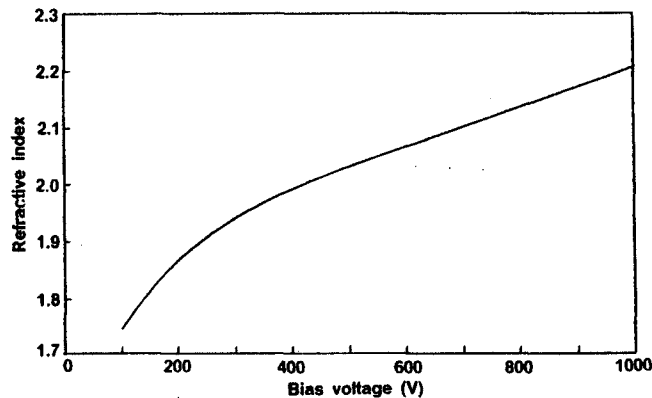


Fig. 15. Refractive index vs. bias voltage for PD a-C:H from benzene source gas (after Koidl *et al.* [12]).

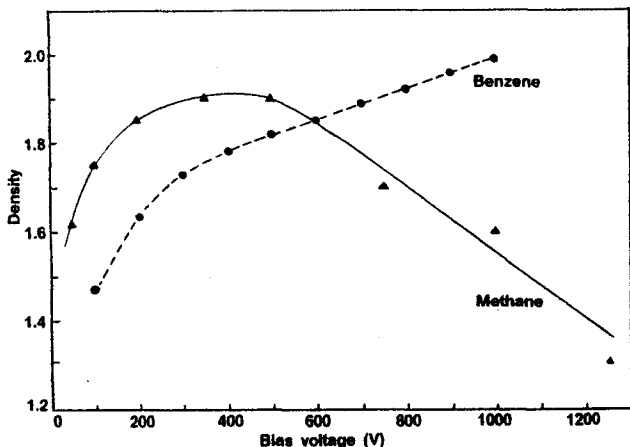


Fig. 16. Density vs. bias voltage for PD a-C:H from methane and benzene source gases (after Tamor [89] and Koidl *et al.* [12]).

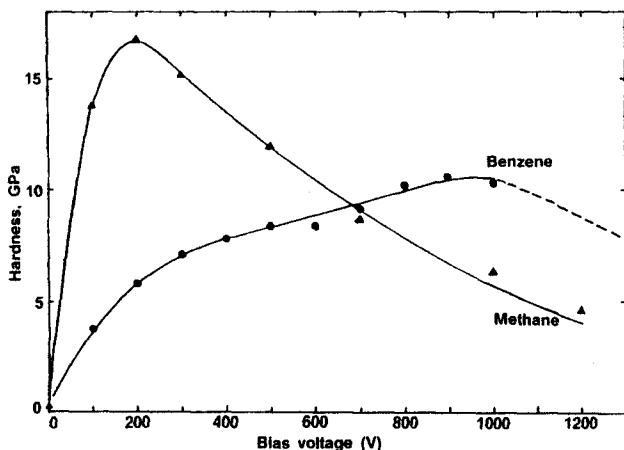


Fig. 17. Hardness vs. bias voltage for PD a-C:H from methane and benzene source gases (after Jiang *et al.* [90] and Koidl *et al.* [12]).

Koidl *et al.* [12] proposed the useful rule that the properties of hard and graphitic a-C:H were independent of the source gas while those of soft a-C:H depended on the source gas. The foundation of this rule is their observation that the source gas is essentially completely decomposed in the plasma at higher bias voltages but not at low bias [44, 45]. Thus Koidl *et al.* [12] noted that the hydrogen content,  $sp^3$  content as determined by IR, optical gap and refractive index were each very similar for hard a-C:H deposited from methane, benzene, *n*-hexane and cyclohexane at  $V_b = 400$  V. In contrast, there are strong differences in the film structures of soft a-C:H, particularly in their pendant (side-chain) groupings, as is seen readily by IR [12, 70]. More detailed comparisons in Figs. 13–17 above show that electronic properties such as the optical gap follow this rule very well but the density and hardness do not, remaining quite different at high bias. The cause of this failure is not understood.

The ability to vary the optical gap and refractive index of PD a-C:H films makes them particularly suitable for protective optical coatings. The films can be prepared at a bias voltage which allows their refractive index to be matched to the substrate. In fact, the dependence on bias and gas pressure  $P$  is quite complex. Bubenzer *et al.* [13] found that the gap varies as  $V_b$  with only a weak pressure dependence, while the refractive index varies as  $V_b P^{-1}$  and the density varies as  $V_b P^{-1/2}$ . The harder a-C:H films only have low absorption in the far IR rather than the optical range, as seen for a typical film in Fig. 6. The C–H vibrational bands create absorption in the near IR. This absorption can be reduced by using fluorinated a-C:H (a-C:H,F) deposited from fluorinated benzenes as shown by Sah *et al.* [92].

The properties of a-C:H depend little on the deposition temperature  $T_d$  provided that it remains below 200 °C. This contrasts with the situation in PD a-Si:H

where  $T_d$  is the key variable, producing sizable changes in the hydrogen content and configuration. Deposition of a-C:H above 200 °C or annealing above 300–500 °C causes a gradual decline in hydrogen content, an increase in  $sp^2$  fraction and a closing of the optical gap owing to graphitization [59, 77, 93–95]. Grill *et al.* [95] observed from the behaviour of the  $1600\text{ cm}^{-1}$  C=C IR mode that internal rearrangements allow graphitization to occur at a lower temperature than hydrogen loss. Grill *et al.* also noted a reduction in residual stress at higher deposition temperatures.

The thermal stability of a-C:H is limited by the loss of hydrogen and the consequent bonding changes. Figure 18 shows typical hydrogen evolution spectra for PD a-C:H films deposited from methane [96] and benzene [97] as a function of bias. Soft a-C:H begins to lose hydrogen at about 300 °C whereas hard a-C:H loses hydrogen at 600–700 °C.

The hydrogen evolution spectra of a-C:H give information on the nature of its network. Consider first the simpler case of a-Si:H. Hydrogen evolves from a-Si:H at two temperatures, roughly 300 and 550 °C [98, 99]. The low temperature evolution is due to weakly bound hydrogen at polymeric or void surface sites. The evolution rate is limited by the recombination rate of two H atoms at the internal surface, and the  $H_2$  molecule subsequently reaches the film surface by permeation along micropores. The high temperature evolution is due to strongly bound hydrogen in the bulk film. Its evolution rate is limited by the diffusion of H atoms across the bulk film. These differences were verified by varying the film thickness and studying isotopic mixing from a-Si:H/a-Si:D film sandwiches. The weakly bound hydrogen content can be minimized by raising  $T_d$ , which gives a compact, impermeable film.

Hydrogen evolution from a-C:H differs in a number of ways. Firstly, the permeability of PD a-C:H depends

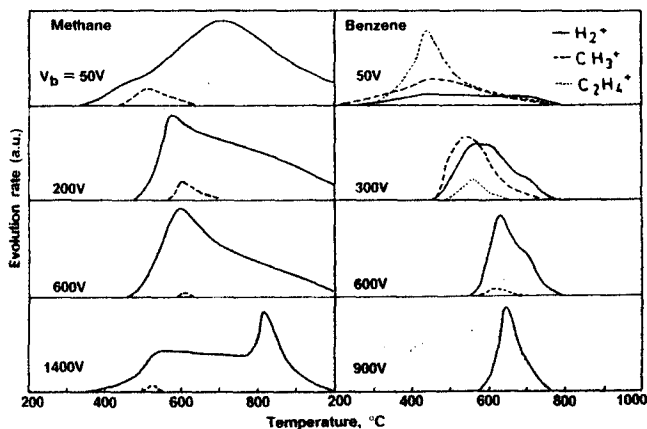


Fig. 18. Hydrogen evolution rate vs. temperature for PD a-C:H derived from methane [96] and benzene [97] as a function of bias voltage.

primarily on the deposition bias voltage. Soft a-C:H is much more permeable to H<sub>2</sub> than hard a-C:H. Secondly, even the relatively impermeable hard a-C:H evolves hydrogen by H<sub>2</sub> permeation through micropores, rather than by the diffusion of H atoms through the bulk solid, according to sandwich studies [97]. A similar effect occurs in a-C:H created by the proton irradiation of graphite [100, 101]. Thirdly, soft a-C:H is sufficiently permeable that hydrogen can even evolve from pendant groups as hydrocarbons rather than as H<sub>2</sub>. This is particularly true of benzene-derived films. Thus hydrogen evolution reveals that the network of a-C:H, even hard a-C:H, is considerably less compact than is possible or than is a-Si:H.

## 6. Mechanical properties

The mechanical properties of diamond-like carbon, *i.e.* its elastic modulus, hardness, friction and wear, are of great interest for its use as a coating. The strength and rigidity of diamond arise from its strong, directional  $\sigma$  bonds. The very high bulk modulus derives largely from its short bond length, because the bulk modulus  $B$  of covalent solids tend to vary with bond length  $R$  as [102]

$$B = B_0 R^{-3.5} \quad (9)$$

The  $sp^3$  bonds of diamond are also exceptionally resistant to angular distortions; a reasonable measure of this is the ratio of shear to bulk modulus,  $S/B$ , which is twice as high in diamond as in other diamond structure crystals such as silicon and germanium, as seen in Table 8.

The mechanical properties of amorphous carbons clearly depend on the strength of their component bonds. Their mechanical properties are inferior to those of diamond because of their finite  $sp^2$  and hydrogen content (Table 1). It is possible to give a firmer theoretical model of these properties, starting with elasticity, the most

tractable. The elasticity of amorphous carbons can be related to the elasticity of the individual bonds and the connectivity or coordination of the network using the constraint-counting model of Phillips [103] and Thorpe [104, 105]. A covalent network of  $N$  atoms can be represented by first-neighbour bond-stretching and bond-bending forces. When the mean coordination  $r$  is low, there are many ways in which the network can be deformed at zero energy cost, *i.e.* leaving bond lengths and bond angles unchanged. The number of these deformations or zero-frequency vibration modes of a network of  $N$  atoms is given by the number of degrees of freedom ( $3N$ ) minus the number of constraints ( $N_{co}$ ). The number of constraints varies with the coordination ( $r$ ). There is one constraint associated with each bond (shared between two atoms) and  $2r-3$  constraints with the angles of each  $r$ -coordinated atom, giving a total of

$$N_{con}(r) = \frac{5}{2}r - 3 \quad (10)$$

per site, except for monovalent atoms such as hydrogen for which

$$N_{con}(1) = \frac{1}{2} \quad (11)$$

The fraction of zero-frequency modes is then given by  $f = 1 - N_{co}/3N$ . Writing  $f = \sum x_r x_r$ , we obtain

$$f = \sum_{r>1} x_r (2 - \frac{5}{6}r) = 2 - \frac{5}{6}\bar{r} \quad (12)$$

where  $x_r$  is the concentration of  $r$ -fold sites and  $\bar{r} = \sum r x_r$  is the mean coordination. Equation (12) shows that a critical coordination or percolation threshold  $r_p$  exists

$$r_p = 2.4 \quad (13)$$

below which the network can be deformed a zero energy cost and is called under-constrained or "floppy". Above  $r_p$  the network is called overconstrained or "rigid". Its modulus then varies as  $(-f)^{1.5}$  or

$$E = E_0 \left( \frac{-f}{-f_0} \right)^{1.5} = E_0 \left( \frac{r-2.4}{r_0-2.4} \right)^{1.5} \quad (14)$$

TABLE 8. Mechanical properties: Comparison of Young modulus, bulk modulus, shear modulus, Poisson ratio, hardness and yield stress

	$E$ (GPa)	$B$ (GPa)	$S$ (GPa)	$\nu$	$H$ (GPa)	$Y$ (GPa)	Reference(s)
Diamond	1050	442	478	0.104	103	59	[2, 108, 116]
PD a-C:H (100 V)	145	52	24	0.4	16	9.7	[90, 113]
PD a-C:H (1 kV)	55	23	31	0.2	6.3	3.1	[90, 113]
a-C (sputtered)	140				15	8	[15]
a-C (MSIB)					20-110	12-65	[27, 38]
Graphite ( $\parallel a$ )	686						[109]
Glassy C (GC10)	29		12.5	0.15	3.0	1.0	[110, 111]
Glassy C (GC20)	32		13.5	0.17	2.2	0.73	[110, 111]
Si	130	97.8	50.9	0.278	10.4	5.0	[112]
a-Si:H	100			0.32	10.0	4.9	[90, 114]

Elastic constants of diamond are calculated from the elastic stiffnesses of McSkimin *et al.* [126].

where  $E_0$  is the modulus of the fully coordinated network,  $r_0=4$  in our case.

Angus and Jansen [106] found that condition (13) for  $r_p$  can still be used for a network containing hydrogen if  $r$  now represents the C-C coordination, by treating each C-H bond as a broken bond contributing no rigidity. This requires substituting  $r \rightarrow r - x_{1,r}/x_r$  in eqn. (10) and  $x_r \rightarrow x_r/(1-x_1)$  in eqn. (12), where  $x_{1,r}$  is the concentration of hydrogen bonded to  $r$ -fold sites, to give

$$f = \sum_{r>1} [(2 - \frac{5}{6}r)x_r + \frac{5}{6}x_{1,r}]/[1-x_1] \quad (12')$$

Indeed, all pendant groups such as  $-\text{CH}_3$  contribute no network rigidity.

The constraint model must also be modified to take into account  $\pi$  bonding. A  $\pi$  bond between two  $\text{sp}^2$  sites as in ethylene adds torsional rigidity to that bond. It therefore adds a half constraint per atom, increasing  $N_{\text{con}}$  from 4.5 to 5 for an  $\text{sp}^2$  site. Thus an  $\text{sp}^2$  C atom is more constrained than a trivalent P atom.

The constraint counting model must clearly be modified to treat graphitic bonding. Graphite is a slippery solid with no rigidity between its layers, despite it having a coordination of three, well above the critical minimum value of  $r_p=2.4$ . The model fails for graphite because of its anisotropic bonding. It is strongly bonded in two dimensions but has only weak van der Waals bonding between the layers. In terms of constraints, graphite uses all of its constraints in maintaining rigid layers and none in its interlayer bonding. A graphite layer of  $N'$  atoms can be treated as an internally rigid disk with  $3N' - 3$  constraints, three for each site minus three for its translational degrees of freedom. Such an internally rigid graphite layer or graphitic cluster embedded in a network at  $N''$  perimeter sites acts like a  $N''$ -fold coordinated site. This adds a further  $(5N''/2 - 3)$  constraints, to give

$$N_{\text{con}}(3) = (3N' - 3) + (\frac{5}{2}N'' - 3) \quad (15)$$

and

$$f_3 = 1 - \frac{1}{3}N_{\text{con}} = \frac{2}{N'} - \frac{5N''}{6N'} \quad (16)$$

$N''$  is typically much less than  $N'$ . For a circular cluster  $N'' \approx 2(\pi N')^{1/2}$  and typically  $N'' \approx 2.5(N')^{1/2}$ , for a compact cluster giving

$$f_3 \approx \frac{2}{N'} - 2.1(N')^{-1/2} \quad (17)$$

This shows that clustering has the effect of raising  $r_p$  for  $\text{sp}^2$  sites and making graphite itself borderline floppy. As clusters tend to be large, we take  $N' \rightarrow \infty$  and

$$f_3 \approx 0 \quad (18)$$

giving finally

$$-f \approx -\frac{x_4 f_4}{1-x_1} = \frac{\frac{4}{3}x_4 - \frac{5}{6}x_{1,4}}{1-x_1} \quad (19)$$

where  $x_{1,4}$  is the fraction of hydrogen bonded to fourfold sites. We thus reach the important conclusion that both graphitic and polymeric bonding tend to reduce rigidity.

The lack of rigidity from graphitic bonding can be confirmed by considering the Young modulus of glassy carbon (Table 8). Its modulus is seen to be only about 5% of the in-plane modulus of graphite [111]. This is consistent with a modulus derived only from the interplane cross links occurring every  $L_a \approx 20$  rings apart, the observed value.

In the two-phase model the network of a-C:H consists of  $\text{sp}^2$  clusters which control the band gap embedded in the  $\text{sp}^3$  phase whose C-C coordination controls the rigidity. Figure 19 shows the Young modulus of PD a-C:H deposited from methane by Jiang *et al.* [90] compared with that calculated from eqns. (14, 19) using the coordination data of Tamor *et al.* [64] for similar films and with  $E_0$  taken from diamond. The agreement is seen to be good. The model shows that  $E$  is small at low bias because of the predominance of polymeric groups and declines again at high bias because of the increasing  $\text{sp}^2$  content. This decline cannot be reproduced unless the  $\text{sp}^2$  sites form clusters which contribute little rigidity.

The effective C-C coordination may be estimated for these films from eqn. (14) giving  $r=2.83$  for the 100 V film and  $r=2.63$  for the 1 kV film. Clearly, these networks have coordinations well below the ideal limit of four but well above  $r_p$ . Angus and Jansen [106] argued that the hydrogen content and  $\text{sp}^2$  content of a-C:H are opti-

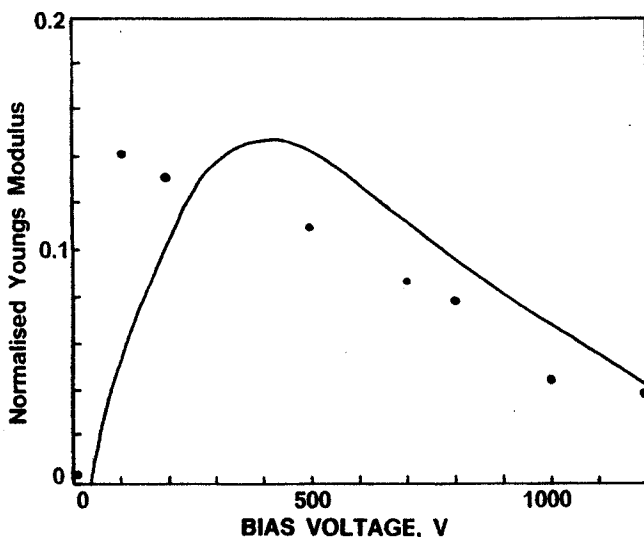


Fig. 19. Young modulus vs. bias voltage for PD a-C:H from methane source gas (after Jiang *et al.* [90]) compared with the theoretical curve.

mized during deposition to give  $\bar{r} \approx 2.4$ , since this is the coordination at which the energy gain from increased bond density might balance the increase in network strain energy. The above derivation suggests that the coordination of the network must exceed 2.4 otherwise it would have no rigidity (or hardness). Happily, for the sake of forming hard carbons, it does. Nevertheless, the low Young modulus of a-C:H compared to that of diamond serves to emphasize that the C-C coordination of PD a-C:H is still relatively low.

The Young modulus of magnetron-sputtered a-C has been found to be 115–141 GPa [15] (Table 8), as high as that of hard PD a-C:H. This material has at most 5%  $sp^3$  sites and little hydrogen. Its rigidity must originate largely from its  $sp^2$  sites. An isotropically bonded threefold-coordinated network would have a modulus of 23% of that of diamond, 230 GPa, from eqn. (14). The observed maximum modulus is 60% of this. It is likely that the rigidity of the  $sp^2$  network arises from a significant interlayer cross-linking, giving it a limited form of isotropic bonding. Indeed,  $E$  does vary with the Raman D intensity and hence with  $L_a$  [15]. A periodic model with cross-linking and a high modulus is the H-6 structure of Tamor [115]. In contrast, it appears that the  $sp^2$  clusters give little rigidity in a-C:H because they are well separated and cannot cross-link.

Hardness is the key parameter of diamond-like carbons of technological relevance. It is measured by indentation and is the pressure over the permanently indented area at a given applied load. Hardness is a measure of the yield stress  $Y$  and is related to  $Y$  by an equation of the form

$$\frac{H}{Y} = 0.07 + 0.6 \ln \left( \frac{E}{Y} \right) \quad (20)$$

This equation is based on an analysis of stress around the indenter tip. The constants in eqn. (20) were found by fitting data for a range of materials (metals, polymers and glasses) which cover a wide range of  $Y/E$  ratios [116, 117]. Equation (20) can be rearranged to give

$$\frac{H}{Y} \approx -0.04 + 0.77 \ln \left( \frac{E}{H} \right) \quad (21)$$

or

$$\frac{H}{Y} \approx 1.8 \quad (22)$$

for material with high  $E/Y$  ratios such as diamond and a-C:H (much lower than the typical factor of 3 for metals).

The yield stress of a metal is controlled by dislocation flow, which gives relatively low values of  $Y/E$ . In contrast, dislocation motion is much more difficult in covalent materials such as diamond and yield tends to occur

by cleavage, giving a high value of  $Y/E$ . The existence of dislocations in amorphous solids is contentious. In any case they are likely to be pinned by the topological and bond length disorder. Hence yield is also expected to occur by cleavage in a-C(:H). The cleavage stress is the stress needed to separate two adjacent planes of atoms of the solid. This in turn can be related to the Young modulus by the Orowan approximation of replacing the interplanar force by a sine function and equating  $E$  to the initial slope to give [109]

$$Y \approx \frac{E}{\pi} \quad (23)$$

Combining this with eqn. (22) gives  $H \approx E/6$ . The values for diamond in Table 8 show that

$$\frac{H}{E} \approx 0.1 \quad (24)$$

is a better approximation.

Hardness measurements on a-C and a-C:H films must ensure that the indent depth does not exceed 10% of the film thickness and must allow for elastic recovery. The limit on indent depth is necessary because the substrate often has a lower hardness than the film. On the other hand, if the penetration is too small, some error arises because of deformation of the indenter tip. The problem of elastic recovery is shown in Fig. 20. The hardness is the average pressure under the indenter, given by the applied load divided by the projected area of contact. In conventional microhardness tests the indent area is measured by imaging after removing the load. However, if there is significant elastic recovery, the area is underestimated and the hardness overestimated. The extreme example is rubber, which apparently has high hardness because indents in it recover totally. Many early hardness measurements on a-C(:H) suffered from this error, giving values up to 60 GPa for a-C:H. The true hardness is found by estimating the area in the loaded condition from the load *vs.* indent depth curve

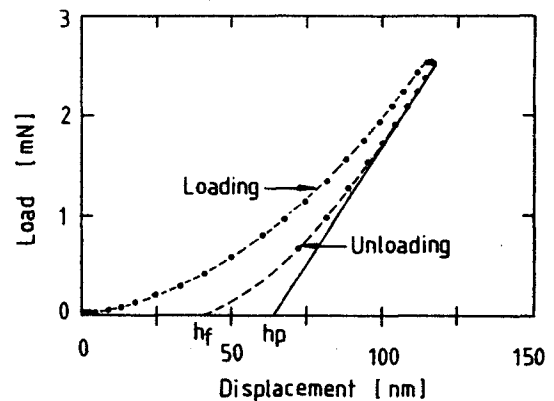


Fig. 20. Load *vs.* depth curve of a nano-indenter on a-C:H.



(Fig. 20). A tangent is drawn to the unloading curve at maximum load and extrapolated to zero load. Its slope is proportional to the Young modulus and it subtends the elastic depth on the displacement axis. The remainder is the plastic depth  $h_p$  needed for hardness. Elastic recovery is significant when  $Y/E$  is not small, such as in covalent solids. Corrected hardness values are typically 30% of uncorrected values.

Hardness values for diamond, PD a-C:H, sputtered a-C and MSIB a-C are given in Table 8. The hardness of PD a-C:H deposited from methane has been measured as a function of bias voltage [90] and that of a-C:H deposited from acetylene as a function of gas pressure [114]. The hardness of sputtered a-C has also been measured as a function of r.f. power [15]. In each case  $H$  is found to scale with the Young modulus according to eqn. (22). This scaling holds despite the bonding changes occurring in the a-C:H and despite the changes in Poisson ratio. The validity of eqn. (22) in a-C(:H) allows the previous model of  $E$  to be extended to cover hardness. The hardness of MSIB a-C has been found to reach values similar to that of diamond [27]. Since diamond is the hardest solid, this is perhaps the simplest demonstration of the high  $sp^3$  content of MSIB a-C. The hardness of MSIB a-C has also been studied as a function of ion energy. It is found to peak at a similar energy as its density [37].

The friction properties of PD a-C:H deposited from ethylene have been measured by Enke and coworkers [118, 119]. The coefficient of friction was found to increase strongly with increasing atmospheric humidity, from a low value of 0.05 at 12% relative humidity to 0.30 at 100% humidity. Diamond itself has a low friction coefficient owing to a combination of its hardness and its low adhesion [120]. The low adhesion arises from the passivation of its surface with stable C-H bonds. The low friction of a-C:H in dry conditions is consistent with this behaviour, but it is difficult to account for the humidity dependence. Grill *et al.* [95] also observed a friction coefficient of the order of 0.3.

Wear of surfaces can arise from several mechanisms such as adhesion, abrasion and tribochemical. Abrasive wear has been observed in a-C:H [121] while abrasive and tribochemical wear have been studied in sputtered a-C [15]. The abrasive wear rate of a surface varies inversely with its hardness. The abrasive wear rate of a-C:H was found to increase by a factor of nearly  $10^6$  as the hardness fell and the hydrogen content varied from 0% to 60%, which is consistent with expectations. Marchon *et al.* [122] observed abrasive and thermochemical wear in sputtered a-C. They found that the abrasive wear rate varied inversely with the Raman  $I(D)/I(G)$  ratio. This is unexpected since hardness has not been previously correlated with this ratio. Tribochemical wear generally arises from the gradual rise in friction

coefficient with wear, leading to temperature rises which trigger graphitization or the oxidation of graphitic components. Marchon *et al.* [122] found the tribochemical wear rate to vary inversely with depression of the Raman G mode frequency. Hirvonen *et al.* [34] observed that the wear of MSIB a-C occurred by a combination of abrasion and cracking. The abrasive wear rate was a factor of 230–290 lower than that of SiC and  $Al_2O_3$  and a factor of 60 lower than that of WC-Co composite, with only diamond itself being lower.

A major problem with a-C(:H) films is that they usually possess substantial intrinsic stress. This limits the adhesion of thicker films. Figure 21 shows the variation in intrinsic stress of PD a-C:H deposited from methane as a function of bias voltage. The stress is compressive at low bias and becomes lower and tensile at high bias. Grill *et al.* [95] noted that the intrinsic stress of PD a-C:H declines at higher deposition temperatures. Sputtered a-C also possesses high stress [123]. The intrinsic stress is very high in MSIB a-C:H. It is compressive and its size has been found to correlate strongly with film density. McKenzie *et al.* [31] propose that the stress induces a coordination transition from  $sp^2$  bonding to metastable  $sp^3$  bonding.

Stress  $\sigma$  leads to the delamination of surface films of thickness  $h$  when the energy density in the film exceeds that which is needed to create two new surfaces of surface energy  $\gamma$ . Adhesion therefore requires [124]

$$\frac{\sigma^2 h}{2E} < 2\gamma \quad (25)$$

It is preferable to rewrite this in terms of strain  $\epsilon$ , since this is continuous across the interface, and to factor out the large variations in Young modulus of the films.

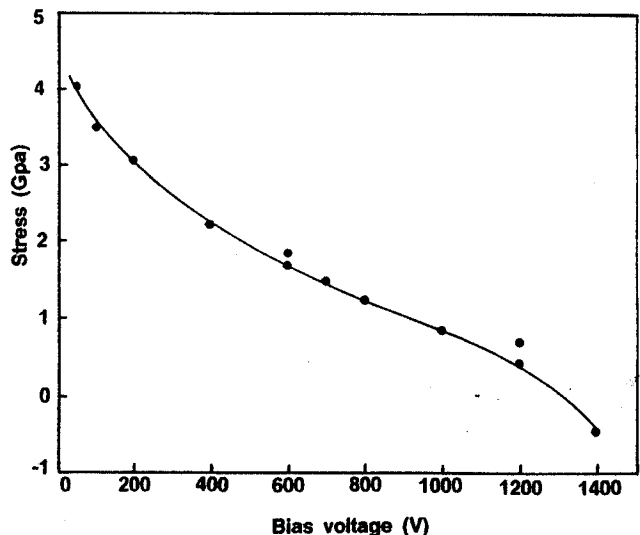


Fig. 21. Residual stress in PD a-C:H deposited from methane (after Jiang *et al.* [113]) (Compressive stress is positive).

Equation (25) becomes

$$h < \frac{4\gamma E}{\epsilon^2} \quad (26)$$

for adhesion, where the numerical factor 4 is approximate. The interfacial energy of a-C(:H) films equals the energy needed to break the bonds across a given plane. Its maximum value is that of diamond,  $5.7 \text{ J m}^{-2}$  [2]. This sets an upper limit on film thickness.

## 7. Summary

Models have been described which allow the electronic and mechanical properties to be related to the underlying atomic structure. The properties of different forms of a-C(:H), particularly PD a-C:H and sputtered a-C have been reviewed. Both PD a-C:H and sputtered a-C are hard coating materials with economic potential. PD a-C:H has better transparency than sputtered a-C but has poorer thermal stability owing to the loss of hydrogen at higher temperatures.

## Acknowledgments

The author is very grateful to P. Gaskell, G. Gilkes, M. Tamor, P. Koidl and Y. Catherine for access to unpublished results and valuable discussions.

## References

- J. C. Angus and C. C. Hayman, *Science*, 241 (1988) 913.
- J. E. Field (ed.), *Properties of Diamond*, Academic, New York, 1979.
- M. W. Geis, *J. Vac. Sci. Technol. A*, 6 (1988) 1953.
- P. Bachmann and H. Lydtin, *MRS Symp. Proc.*, 165 (1990) 181.
- H. Tsai and D. B. Bogy, *J. Vac. Sci. Technol. A*, 5 (1987) 3287.
- S. Aisenberg and R. Chabot, *J. Appl. Phys.*, 42 (1971) 2953.
- E. G. Spencer, P. H. Schmidt, D. C. Joy and F. J. Sansalone, *Appl. Phys. Lett.*, 29 (1976) 118.
- J. C. Angus, P. Koidl and S. Domitz, in J. Mort (ed.), *Plasma Deposited Thin Films*, CRC Press, Boca Raton 1986.
- Y. Catherine, in R. E. Clausing *et al.* (eds.), *Proc. NATO ASI on Diamond and Diamond-like Carbon Films*, Plenum, New York, 1991.
- J. C. Angus, J. E. Stultz, P. J. Schiller, J. R. McDonald, M. J. Mirtlich and S. Domitz, *Thin Solid Films*, 118 (1984) 311.
- L. Holland and S. M. Ojha, *Thin Solid Films*, 38 (1976) L17; 40 (1977) L31; 48 (1978) L15; 58 (1979) 107.
- P. Koidl, C. Wild, B. Dischler, J. Wagner and M. Ramsteiner, *Mater. Sci. Forum*, 52 (1990) 41.
- A. Bubbenzer, B. Dischler, G. Brandt and P. Koidl, *J. Appl. Phys.*, 54 (1983) 4590.
- N. Savvides, *J. Appl. Phys.*, 59 (1986) 4133.
- N. H. Cho, K. M. Krishnan, D. K. Vries, M. D. Rubin, C. B. Hopper, B. Brushan and D. B. Bogy, *J. Mater. Sci.*, 5 (1990) 2543.
- S. M. Rossnagel, M. A. Russak and J. J. Cuomo, *J. Vac. Sci. Technol. A*, 5 (1987) 2150.
- F. Jansen, M. Machonkin, S. Kaplan and S. Hark, *J. Vac. Sci. Technol. A*, 3 (1985) 605.
- J. J. Cuomo, J. P. Doyle, J. Bruley and J. C. Liu, *Appl. Phys. Lett.*, 58 (1991) 466.
- C. Weissmantel, *Thin Solid Films*, 92 (1982) 55.
- C. Weissmantel, *Proc. Eur. MRS*, 17 (1987) 49.
- A. Richter, H. J. Scheibe, W. Pompe, K. W. Brzezinka and I. Muhling, *J. Non-cryst. Solids*, 88 (1990) 131.
- F. Davanloo, E. M. Juengerman, D. R. Jander, T. J. Lee and C. B. Collins, *J. Appl. Phys.*, 67 (1990) 2081.
- J. Robertson, *Adv. Phys.*, 35 (1986) 317.
- J. Robertson, *Mater. Sci. Forum*, 52 (1990) 125.
- J. Robertson, in R. Clausing *et al.* (eds.), *Proc. NATO ASI on Diamond and Diamond-like Carbon Films*, Plenum, New York, 1991.
- J. Robertson, *J. Non-cryst. Solids*, in press.
- P. J. Martin, S. W. Filipczuk, R. P. Netterfield, J. S. Field, D. F. Whittall and D. R. McKenzie, *J. Mater. Sci. Lett.*, 7 (1988) 410.
- S. D. Berger, D. R. McKenzie and P. J. Martin, *Philos. Mag. Lett.*, 57 (1988) 285.
- D. C. Green, D. R. McKenzie and P. B. Lukins, *Mater. Sci. Forum*, 52 (1990) 103.
- D. R. McKenzie, D. C. Green, P. D. Swift, D. J. H. Cockayne, P. J. Martin, R. P. Netterfield and W. G. Sainty, *Thin Solid Films*, 193 (1990) 418.
- D. R. McKenzie *et al.*, *Diamond Relat. Mater.*, 1 (1991) 51.
- P. H. Gaskell, A. Saeed, P. C. Chieux and D. R. McKenzie, *Phys. Rev. Lett.*, 67 (1991) 773.
- I. I. Aksenov, S. I. Vakula, V. G. Padalka, R. E. Strelitski and V. M. Khoroshikh, *Sov. Phys. — Tech. Phys.*, 25 (1980) 1164.
- J. P. Hirvonen, R. Lappalainen, J. Koskinen, A. Antilla, T. R. Jervis and M. Trkula, *J. Mater. Res.*, 5 (1990) 2524.
- G. M. W. Kroesen, D. C. Schram and M. J. F. van de Sande, *Plasma Chem. Proc.*, 10 (1990) 49.
- H. Kersten and G. M. W. Kroesen, *J. Vac. Sci. Technol. A*, 8 (1990) 38.
- A. Antilla, J. Koskinen, R. Lappalainen, J. P. Hirvonen, D. Stone and C. Paszkiet, *Appl. Phys. Lett.*, 50 (1987) 132.
- J. Koskinen, *J. Appl. Phys.*, 63 (1988) 2094.
- J. P. Hirvonen, J. Koskinen, R. Lappalainen and A. Antilla, *Mater. Sci. Forum*, 52 (1990) 197.
- T. Miyazawa, S. Misawa, S. Yoshida and S. Gonda, *J. Appl. Phys.*, 55 (1984) 188.
- J. Ishikawa, Y. Takeiri, K. Ogawa and T. Takagi, *J. Appl. Phys.*, 61 (1987) 2509.
- Y. Lifshitz, S. R. Kasi and J. W. Rabalais, *Phys. Rev. Lett.*, 62 (1989) 1290.
- Y. Catherine and P. Couderc, *Thin Solid Films*, 144 (1986) 265.
- Y. Catherine and A. Pastol, *Proc. Eur. MRS*, 17 (1987).
- J. Wagner, C. Wild, F. Pohl and P. Koidl, *Appl. Phys. Lett.*, 48 (1986) 106.
- C. Wild, P. Koidl and J. Wagner, *Proc. Eur. MRS*, 17 (1987) 137.
- J. W. Zou, K. Reichelt, K. Schmidt and B. Dischler, *J. Appl. Phys.*, 65 (1989) 3914.
- J. W. Zou, K. Schmidt, K. Reichelt and B. Dischler, *J. Appl. Phys.*, 67 (1990) 487.
- J. Wagner, C. Wild, R. Lorcher, R. E. Sah and P. Koidl, in R. E. Clausing *et al.* (eds.), *Proc. NATO ASI on Diamond and Diamond-like Carbon Films*, Plenum, New York, 1991.
- R. Lorcher, C. Wild and P. Koidl, *Surf. Coat. Technol.*, 47 (1991) 69.
- A. Matsuda, *J. Non-cryst. Solids*, 59 (1983) 767.
- K. Tanaka and A. Matsuda, *Mater. Sci. Rep.*, 2 (1987) 139.
- W. Varhue and P. Pastel, *J. Mater. Res.*, 5 (1990) 2441.
- J. C. Angus, *Proc. Eur. MRS*, 17 (1987) 179.

- 53 J. Robertson and E. P. O'Reilly, *Phys. Rev. B*, 35 (1987) 2946.
- 54 J. L. Bredas and G. B. Street, *J. Phys. C: Solid State Phys.*, 18 (1985) L651.
- 55 G. Galli, R. M. Martin, R. Car and M. Parinello, *Phys. Rev. Lett.*, 62 (1989) 555.
- 56 J. Hauser, *J. Non-cryst. Solids*, 23 (1977) 21.
- 57 B. Dischler, A. Bubenzer and P. Koidl, *Appl. Phys. Lett.*, 42 (1983) 636.
- 58 M. A. Petrich, *Mater. Sci. Forum*, 52 (1989) 387.
- 59 B. Dischler, A. Bubenzer and P. Koidl, *Solid State Commun.*, 48 (1983) 105.
- 60 B. Dischler, *Proc. Eur. MRS*, 17 (1987) 189.
- 61 S. Kaplan, F. Jansen and J. Machonkin, *Appl. Phys. Lett.*, 47 (1985) 750.
- 62 A. Grill, B. S. Meyerson, V. V. Patel, J. A. Reimer and M. A. Petrich, *J. Appl. Phys.*, 61 (1987) 2874.
- 63 K. C. Bustillo, M. A. Petrich and J. A. Reimer, *Chem. Mater.*, 2 (1990) 202.
- 64 M. A. Tamor, W. C. Vassell and K. R. Carduner, *Appl. Phys. Lett.*, 58 (1991) 592.
- 65 R. H. Jarman, G. J. Ray, R. W. Standley and G. W. Zajac, *Appl. Phys. Lett.*, 49 (1986) 1065.
- 66 J. Fink, T. Muller-Heinzerling, J. Pfluger, A. Bubenzer, P. Koidl and G. Grececius, *Solid State Commun.*, 47 (1983) 887.
- 67 Y. Wang, H. Chen, R. W. Hoffman and J. C. Angus, *J. Mater. Res.*, 5 (1990) 2378.
- 68 J. Fink, T. Muller-Heinzerling, J. Pfluger, B. Scheerer, B. Dischler, P. Koidl, A. Bubenzer and R. E. Sah, *Phys. Rev. B*, 30 (1984) 4713.
- 69 M. A. Tamor and C. H. Wu, *J. Appl. Phys.*, 67 (1990) 1007.
- 70 M. A. Tamor, C. H. Wu, R. O. Carter and N. E. Lindsey, *Appl. Phys. Lett.*, 55 (1989) 1388.
- 71 C. Gao, Y. Y. Wang, A. L. Ritter and J. R. Dennison, *Phys. Rev. Lett.*, 62 (1989) 945.
- 72 Y. Mizokawa, T. Miyasato, S. Nakamura, K. M. Geib and C. W. Williamson, *J. Vac. Sci. Technol. A*, 5 (1987) 2809.
- 73 R. E. Shroder, R. J. Nemanich and J. T. Glass, *Phys. Rev. B*, 41 (1990) 3738.
- 74 F. Tuinstra and J. L. Koenig, *J. Chem. Phys.*, 53 (1970) 1126.
- 75 R. J. Nemanich and S. A. Solin, *Phys. Rev. B*, 20 (1979) 392.
- 76 N. Wada and S. A. Solin, *Physica B*, 105 (1981) 353.
- 77 N. Wada, P. J. Gaczi and S. A. Solin, *J. Non-cryst. Solids*, 35 (1980) 543.
- 78 M. Ramsteiner and J. Wagner, *Appl. Phys. Lett.*, 51 (1987) 1355. J. Wagner, M. Ramsteiner, C. Wild and P. Koidl, *Phys. Rev. B*, 40 (1989) 1817.
- 79 M. A. Tamor, J. A. Haire, C. H. Wu and K. C. Hass, *Appl. Phys. Lett.*, 54 (1989) 123.
- 80 M. Yoshikawa, G. Katagiri, H. Ishitani and T. Akamatsu, *Appl. Phys. Lett.*, 52 (1988) 1639; *J. Appl. Phys.*, 64 (1988) 6464.
- 81 D. Beeman, J. Silverman, R. Lynds and M. R. Anderson, *Phys. Rev. B*, 30 (1984) 870.
- 82 D. F. R. Mildner and J. M. Carpenter, *J. Non-cryst. Solids*, 47 (1982) 391.
- 83 B. T. Boiko, L. S. Palantik and A. S. Deveryanchenko, *Sov. Phys.—Dokl.*, 13 (1968) 237.
- 84 J. Kakinoki, K. Katada, T. Hanawa and T. Ino, *Acta Crystallogr.*, 13 (1960) 171.
- 85 D. R. McKenzie, L. C. Botten and R. C. McPhedran, *Phys. Rev. Lett.*, 51 (1983) 280.
- 86 R. J. Newport, P. J. R. Honeybone, S. P. Cottrell et al., *Surf. Coat. Technol.*, 47 (1991) 668.
- 87 F. Li and J. S. Lannin, *Phys. Rev. Lett.*, 65 (1991) 1905.
- 88 H. Pan, M. Pruski, B. C. Gerstein, F. Li and J. S. Lannin, *Phys. Rev. B*, in press.
- 89 M. A. Tamor, personal communication, 1991.
- 90 X. Jiang, K. Reichelt and B. Stritzker, *J. Appl. Phys.*, 66 (1989) 5805.
- 91 C. Weissmantel, K. Bewilogua, K. Breuer, D. Dietrich, U. Ebersbach, H. J. Erler, R. Rau and G. Reisse, *Thin Solid Films*, 96 (1982) 31.
- 92 R. E. Sah, B. Dischler, A. Bubenzer and P. Koidl, *Appl. Phys. Lett.*, 46 (1985) 739.
- 93 T. Datta, J. A. Woollam and W. Notohamiprodjo, *Phys. Rev. B*, 40 (1989) 5956.
- 94 F. W. Smith, *J. Appl. Phys.*, 55 (1984) 764.
- 95 A. Grill, V. Patel and B. S. Meyerson, *J. Mater. Res.*, 5 (1990) 2531.
- 96 X. Jiang, W. Beyer and K. Reichelt, *J. Appl. Phys.*, 68 (1990) 1378.
- 97 Ch. Wild and P. Koidl, *Appl. Phys. Lett.*, 51 (1987) 1506.
- 98 W. Beyer and H. Wagner, *J. Appl. Phys.*, 53 (1982) 8745.
- 99 W. Beyer and H. Wagner, *J. Non-cryst. Solids*, 59 (1983) 161.
- 100 W. Moller and B. M. U. Scherzer, *Appl. Phys. Lett.*, 50 (1987) 1870.
- 101 G. Kogel, D. Schodlbauer, W. Triftshauer and J. Winter, *Phys. Rev. Lett.*, 60 (1988) 1550.
- 102 M. L. Cohen, *Phys. Rev. B*, 32 (1985) 7988.
- 103 J. C. Phillips, *J. Non-cryst. Solids*, 34 (1979) 153.
- 104 M. F. Thorpe, *J. Non-cryst. Solids*, 57 (1983) 355.
- 105 H. He and M. F. Thorpe, *Phys. Rev. Lett.*, 54 (1985) 2107.
- 106 J. C. Angus and F. Jansen, *J. Vac. Sci. Technol. A*, 6 (1988) 1778.
- 107 R. J. Nemanich, G. Lucovsky and S. A. Solin, *Solid State Commun.*, 23 (1977) 117.
- 108 C. A. Brookes, *Philos. Mag. A*, 43 (1981) 529.
- 109 A. Kelly and N. H. MacMillan, *Strong Solids*, Oxford University Press, Oxford, 1986.
- 110 H. M. Hawthorne, *Carbon*, 13 (1975) 215.
- 111 J. X. Zhao, R. C. Bradt and P. L. Walker, *Carbon*, 23 (1985) 15.
- 112 V. I. Trefilov and Y. V. Milman, *Sov. Phys.—Dokl.*, 8 (1964) 1240.
- 113 X. Jiang, J. W. Zou, K. Reichelt and P. Grunberg, *J. Appl. Phys.*, 66 (1989) 4729.
- 114 X. Jiang, K. Reichelt and B. Stritzker, *J. Appl. Phys.*, 68 (1990) 1018.
- 115 M. A. Tamor and K. C. Hess, *J. Mater. Res.*, 5 (1990) 2273.
- 116 D. Tabor, *Rev. Phys. Technol.*, 1 (1970) 145.
- 117 S. S. Chiang, D. B. Marshall and A. G. Evans, *J. Appl. Phys.*, 53 (1982) 298.
- 118 K. Enke, *Thin Solid Films*, 80 (1981) 227.
- 119 K. Enke, H. Dimigen and H. Hubsch, *Appl. Phys. Lett.*, 36 (1980) 291.
- 120 D. Tabor, in J. E. Field (ed.), *Properties of Diamond*, Academic, New York, 1979.
- 121 F. Jansen and M. A. Machonkin, *Thin Solid Films*, 140 (1986) 227.
- 122 B. Marchon, N. Heiman, M. R. Khan, A. Lautie, J. W. Ager and D. K. Veirs, *J. Appl. Phys.*, 69 (1991) 5748.
- 123 M. Rubin, C. B. Hopper, N. H. Cho and B. Bhushan, *J. Mater. Res.*, 5 (1990) 2538.
- 124 J. Robertson and M. I. Manning, *Mater. Sci. Technol.*, 6 (1990) 81.
- 125 M. F. Ashby and D. R. H. Jones, *Engineering Materials*, Pergamon, Oxford, 1980, pp. 58, 78.
- 126 H. J. McSkimin, P. Andreatch and P. Glynn, *J. Appl. Phys.*, 43 (1972) 985.